Fluorophosphates and fluorosulfates cathode materials: Progress towards high energy density sodium-ion battery

Mohammed Hadouchi[1,2] (✉), Jingrong Hou[2], Toshinari Koketsu[2,3], Abdelilah Lahmar[4], and Jiwei Ma[2] (✉)

[1] *Laboratoire de Chimie Appliquée des Matériaux, Centre des Sciences des Matériaux, Faculty of Science, Mohammed V University in Rabat, Avenue Ibn Battouta, BP 1014, Rabat, Morocco*

[2] *Shanghai Key Laboratory for R&D and Application of Metallic Functional Materials, Institute of New Energy for Vehicles, School of Materials Science and Engineering, Tongji University, Shanghai 201804, China*

[3] *Battery Materials Development Section, Business Creation Sector R&D Center, Mitsui Mining & Smelting Co., Ltd., 362-0021 Saitama, Japan*

[4] *Laboratoiry of Condensed Matter Physics, University of Picardie Jules Verne, 33 Rue Saint-Leu 80039, Amiens, France*

ABSTRACT

The rapid diffusion of renewable energy boosts the wide deployment of large-scale energy storage system. With the low cost and high crustal abundance, sodium-ion battery (SIB) technology is expected to become a dominant technology in that area in the future. Toward the practical application, novel cathode materials are urged to develop that show high energy density without sacrificing their cost and benignity to the environment. While the years of many studies, this still remains a huge challenge to battery scientists. In this review, we discuss recent breakthroughs in SIB cathode materials with high energy density, namely fluorphosphates and fluorosulfates. The design of materials, the crystal structure, the electrochemical performance, and the underlaying intercalation mechanism are systematically reviewed. Useful strategies and research directions are also provided to advance future high-energy, low-cost, and ecofriendly cathode materials for next generation SIB.

KEYWORDS

fluorophosphates, fluorosulfates, crystal structure, intercalation mechanism, high energy density, sodium-ion battery

1   Introduction

Followed by the success of lithium-ion battery (LIB) commercialization in the portable electronics market, rechargeable batteries are expected to be applied in the larger-scale devices including electromobility (e-mobility) and stationary energy storage system (ESS) [1–5]. In those applications, one of the largest concerns is the abundance, cost, and environmental issue of raw materials including the battery cell components. For example, in the near future, vulnerable supply of minor metals such as Co and Li can largely impede the diffusion of LIB. Also, mining those metals accompanies serious environmental degradation. It is hard to solve those problems within LIB systems, and therefore, the development of advanced batteries beyond Li is highly desired. In this context, sodium-ion battery (SIB) is a potential alternative choice [6–12]. As the second lightest alkali metal, Na possesses similar physicochemical properties as Li. So, it is expected to build batteries with the same architecture of the LIBs rocking-chair mechanisms. On the earth, Na is far more plentiful (Na: 23,000 ppm vs. Li: 20 ppm) with the distribution worldwide in seawater. More importantly, recent studies revealed that cathode active materials for SIB can be designed without Co or other minor metals. Cu current collector can also be substituted for low-cost Al foils. Those advantages of SIB will become more and more prominent, and SIB will become highly competitive with the spread of rechargeable batteries in the large-scale applications.

However, because the Na reduction potential (−2.7 V vs. standard hydrogen electrode (SHE)) is 300 mV higher than Li (−3.0 V vs. SHE), the deployment of novel high working voltage cathode materials is still the one of primary research directions [13–17]. Roughly speaking, two types of materials are mostly expected to be the cathode for SIB, including layered oxides and polyanionic compounds. Although layered oxides usually exhibit larger capacities, but their operation voltage is relatively low and cyclability is not high. Meanwhile, polyanionic compounds, especially with XO_4^{n-} anions (with X = P and S, PO_4^{3-} and SO_4^{2-}), are usually have robust structures, showing longer cyclability. Besides, operating voltages are often greater than for oxides because of the polyanions' inductive effect [18–21], yielding the increase of the ionic character for the transition metal–oxygen (M–O) bond, thus raising the redox potential [22]. In other words, high electronegativity of XO_4^{n-} weaken the M–O bond, resulting in high operating voltage. Furthermore, introducing electronegative anions, such as F^-, namely PO_4F^{4-} and SO_4F^{3-} [23–32], can also increase the redox potential. Those polyanionic compounds are quite rich in polymorphs and often possess complicated structures. They are also dependent on their synthetic route, temperature, redox center metals, and the substituted electronegative anions. In summary, the advantages of polyanionic materials over layered oxides are the following: (i) Polyanionic materials exhibit a very versatile and adaptable structure, one can mention, phosphates, sulfates, vanadates, and mixed anions, with

various redox centers (Fe, V, Ti, Mn, Ni, Co,...), (ii) polyanionic unit permits fast ion conduction within the crystal framework, (iii) stabilizes the operative redox potentials of the involved transition metals, (iv) preserve high structural stability during sodium ion insertion and extraction, and (v) produces higher redox potential due to strong inductive effect.

Therefore, it is highly beneficial to review various polymorphs including commercially unviable metals such as Co and V, and to understand the relationship of structure and electrochemical activity. In addition, those polyanionic compounds usually show very low electrical conductivities at pristine state, and electrochemical activities, especially high-rate performance and cyclability, are very poor. So, the engineering in the morphology control, particle-size, doping, and supporting carbon materials is necessary to unlock the superior the intrinsic performances of fluorophosphate and fluorosulfates. In the current review, we summarize the recent progresses in polyanionic materials towards high energy density SIB, particularly focusing on Na_2MPO_4F (M = Mn, Fe, and Co), $NaVPO_4F$, $Na_3V_2(PO_4)_2F_3$ (NVPF), and $NaFeSO_4F$. We outline details on the materials design, crystal structure, electrochemical performance, and underlaying intercalation mechanism. Finally, we explore important insights and research directions to design low-cost and ecofriendly polyanionic cathode materials for high energy density SIB.

2 Fluorophosphates

2.1 Na_2MPO_4F (M = Fe, Mn, and Co) fluorophosphates

Na_2FePO_4F, orthorhombic *Pbcn*. Fe is the most ecofriendly, low cost, and abundant in the common transition metal elements. In 2007, Nazar's group firstly reported the structure of Na_2FePO_4F and the characterized electrochemical Li-ion intercalation behavior [33, 34]. The structure is layered structure, and is isostructural to previously reported mixed-anion phosphates such as Na_2FePO_4OH [35] and Na_2CoPO_4F [36]. Its crystal framework consists of chains formed by F-bridged bioctahedral $Fe_2O_7F_2$, being linked through PO_4 groups to produce the layer structure. Na atoms are situated at two different positions (Na1 and Na2)

located between those layers, forming two-dimensional (2D) Na-ions migration paths. They prepared Na_2FePO_4F nanopowder with 1%–3% carbon coating (Na_2FePO_4F/C) via sol–gel method and solid-state method. Rietveld refinement confirmed the pure phase (Fig. 1(a)), and the scanning electron microscopy (SEM) images of the sample elaborated by sol–gel process (Fig. 1(b)) revealed the uniform particles distribution with the average size of 200 nm. Besides, they chemically oxidized Na_2FePO_4F and obtained pure desodiated parent phase, $NaFePO_4F$. Na-ion extraction occurred only from Na2 crystallographic site but not from Na1 site, and the Rietveld refinement showed that volume contraction upon desodiation was only 3.7%. The electrochemical Li intercalation was tested, and 135 mAh·g⁻¹ capacity was attained with the good cycling performance.

Reversible Na-ion intercalation into Na_2FePO_4F was firstly studied by Komaba's group [37]. They prepared a Na_2FePO_4F/C via solid-state process under N_2 atmosphere at 650 °C for 10 h using ascorbic acid as the coating source. Structural investigation of Na_2FePO_4F using X-ray diffraction (XRD), SEM, and transmission electron microscopy (TEM) images revealed the formation of the nano-sized Na_2FePO_4F particles. A Na/Na_2FePO_4F half-cell with 1 M $NaClO_4$ in propylene carbonate/fluoroethylene carbonate (PC/FEC) electrolyte was conducted for the electrochemical testing. A capacity of 110 mAh·g⁻¹ was obtained within 2.0–3.8 V_{Na} at 6.2 mA·g⁻¹ at room temperature (RT) (Fig. 1(c)), which is ca. 90% of theoretical capacity. Two low-polarization voltage plateaus were shown at 3.06 and 2.91 V_{Na} during both charge and discharge process, and 75% of reversible capacity was reported after 20 cycles. It also showed acceptable rate capability (Figs. 1(c) and 1(d)).

For the practical application, the rate capability and cyclability need to be further enhanced. Optimizing the morphology such as the reduction of particle size and shape engineering of Na_2FePO_4F/C using different synthesis routes are the common techniques [38–41]. For instance, Langrock et al. prepared hollow 500 nm-sized Na_2FePO_4F/C spheres via ultrasonic spray pyrolysis [42]. It maintained 80% of the initial capacity over 750 cycles at 1 C. Yan et al. designed Na_2FePO_4F/carbon nanotube (CNT) via a layer-by-layer (LbL) assembly method [43]. It offered a specific
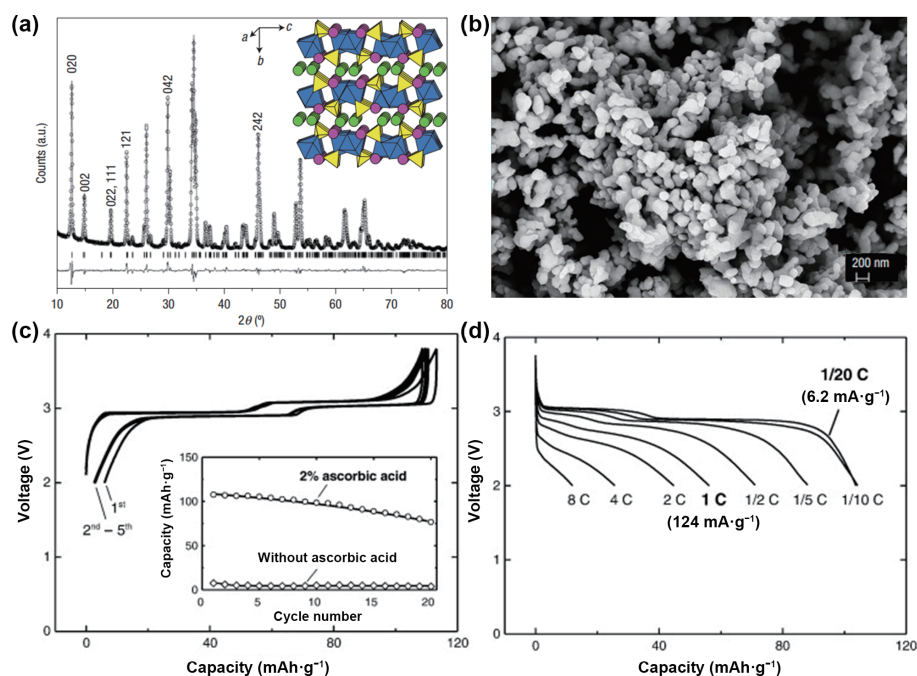

Figure 1 (a) XRD of Na_2FePO_4F and crystal structure of Na_2FePO_4F. (b) An overview SEM image of Na_2FePO_4F. Reproduced with permission from Ref. [33], © Nature Publishing Group 2007. (c) Charge–discharge cycles of a Na/Na_2FePO_4F cell at 6.2 mA·g⁻¹. Evaluation of the effect of ascorbic acid during the preparation is given in the inset. (d) C-rate characteristics of carbon-coated Na_2FePO_4F. Reproduced with permission from Ref. [37], © Elsevier B.V. 2011.

capacity of 100 mAh·g^{-1} at 0.4 C, having 74% of capacity retention over 400 cycles [43]. Recently, Deng et al. synthesized Na$_2$FePO$_4$F/C using a green route strategy [39], featuring a high rate performance with long cyclability. Furthermore, Wang et al. employed electrospinning technique to prepare nanosized Na$_2$FePO$_4$F particles inserted into porous N-doped carbon nanofibers (CNFs) [41], demonstrating a high capacity of ~ 118 mAh·g^{-1} at 0.1 C with improved rate capability up to 20 C and ultralong cyclability over 2000 cycles.

To understand the underlying Na-ions intercalation mechanisms of Na$_2$FePO$_4$F, Danielle et al. studied the chemical shift of Na$^+$ in Na$_2$FePO$_4$F/C during charge–discharge process using *ex-situ* ^{23}Na nuclear magnetic resonance (NMR) [44]. The presence of two distinct phases over the charge process suggested that Na extraction followed a two-phase reaction mechanism. Moreover, they investigated the Na-ion exchange rate between Na1 and Na2 using 2D exchange spectroscopy (2D EXSY). It showed that Na1 and Na2 in Na$_2$FePO$_4$F are unexchangeable at RT. Recently, Li et al. further confirmed that two-phase reaction mechanisms by combining multiple techniques of *ex-situ* NMR, XRD, and density-functional theory (DFT) calculation [45]. Also, DFT calculation suggested that the formed phase upon charge, Na$_{1.5}$FePO$_4$F, adopts to monoclinic system (*P*2$_1$/*c*), proving the previous experimental results by Nazar's group [33].

Na$_2$MnPO$_4$F. In contrast to 2D framework of Na$_2$FePO$_4$F, Mn-based fluorophosphate crystallizes with the three-dimensional (3D) framework in monoclinic system (*P*2$_1$/*n*) [46]. 3D diffusion tunnels desirably facile Na-ions diffusion, and superior electrochemical performance was anticipated. Despite those structural advantages, Tarascon's group [47] and Nazar's group [34] revealed that electrochemical activities of Na$_2$MnPO$_4$F for Na-ion intercalation were extremely poor. In order to boost the electrochemical activities, Zhong et al. prepared Na$_2$MnPO$_4$F/C by ball milling and pyrolytic method [48]. The specific capacity was improved to ~ 120 mAh·g^{-1} in the 1st cycle, and a reasonable cyclability was also obtained. The enhanced electrochemical activity was due to the small particle size (10–30 nm) and carbon coating effect. Some researchers followed these strategies in order to further improve the performances [49–51]. Still, the electrochemical performance of Na$_2$MnPO$_4$F/C remains unsatisfactory for the practical application, and the rational design of Na$_2$MnPO$_4$F electrode beyond those strategies will be favorably proposed that can unlock the attractive high-voltage performance.

Na$_2$CoPO$_4$F. Being isostructural to Na$_2$FePO$_4$F, Co-based phase shows layered structure. It is consisted of the accumulation of [CoPO$_4$F]$_\infty$ layers and Na$^+$ cations are hosted in inter-layers space [36]. The synthesis and electrochemical behavior of Na$_2$CoPO$_4$F were firstly reported by Nazar's group [34]. They obtained Na$_2$CoPO$_4$F via several route of hydrothermal, sol–gel, and solid-state synthesis. Although Na-ion intercalation was irreversible at the preliminary study, the working potential of Na$_2$CoPO$_4$F using the redox of Co$^{2+/3+}$ reaches 4.8 V$_{Na}$, being the highest among its homologs Na$_2$MPO$_4$F (M = Fe, Co, and Mn), and largely attracted attention. In order to enhance electrochemical activity, Kubota et al. elaborated Na$_2$CoPO$_4$F/C via solid-state method [52]. A specific capacity of 100 mAh·g^{-1} for the 1st charge–discharge process was attained. Notably, the discharge curve showed a flat plateau at relative high voltage of 4.3 V$_{Na}$, reaching high energy density of 407 Wh·kg^{-1}. However, cyclability was poor and needs to be further improved. Zou et al. prepared Na$_2$CoPO$_4$F/C using spray-drying technique and sintering at high temperature [53]. A discharge capacity of 107 mAh·g^{-1} with a working voltage of 4.3 V$_{Na}$ was obtained. Although it showed relatively good rate performance, it still suffered from low cyclability. Moreover, it is worthwhile noting

that no electrochemical activity was observed for Na$_2$NiPO$_4$F below 5.0 V$_{Na}$ [34].

2.2 V-based fluorophosphates

NaVPO$_4$F, tetragonal *I*4/*mmm*. Barker et al. firstly synthesized and investigated the electrochemical Na-ion insertion activity [54, 55]. It can be elaborated via various synthesis routes including hydrothermal, ion-exchange, and solid-state methods. A discharge capacity of 101 mAh·g^{-1} was reported for Li-ion intercalation. Additionally, they tested full-cell using hard carbon as the anode. For the first cycle, it displayed a specific capacity of ~ 82 mAh·g^{-1} with a working voltage of 3.7 V$_{Na}$. The discharge capacity retention rate was less than 50% after 30 cycles, and the capacity degradation was very significant.

Doping of hetero transition metals is a widely used strategy in V-based fluorophosphate. Zhuo et al. synthesized the Cr-doped NaV$_{1-x}$Cr$_x$PO$_4$F (*x* = 0, 0.04, and 0.08) samples using solid-state method [56]. XRD showed that all compounds were crystallized in the monoclinic symmetry (*C*2/*c*). The electrochemical tests demonstrated that Cr-doped materials had superior cycle stability than undoped materials, having a 20-cycle capacity retention rate of ~ 91% with a capacity of ~ 83 mAh·g^{-1}. Liu et al. prepared Al-doped NaV$_{1-x}$Al$_x$PO$_4$F (*x* = 0 and 0.02) samples by solid-state reaction [57]. A specific capacity of ~ 80 mAh·g^{-1} was obtained and retained 85% of capacity over 30 cycles, exhibiting enhanced electrochemical performances. Zhao et al. synthesized tetragonal NaVPO$_4$F (*I*4/*mmm*) via sol–gel method [58]. It showed the improved electrochemical performances when used in Li-ion cells. Combining thermal analysis of thermo-gravimetric/differential scanning calorimetry (TG/DSC) and XRD revealed that NaVPO$_4$F phase gradually shifted from monoclinic to tetragonal upon the elevation of temperatures from 700 to 750 °C. The tetragonal NaVPO$_4$F showed a discharge plateau at 3.6 V$_{Li}$, and after 100 cycles at C/4 and 2 C rates, the discharge capacity retentions were ~ 99% and 83%, respectively. In order to boost the electroconductivity and electrochemical activity, Lu et al. prepared NaVPO$_4$F/C by solid-state reaction [59]. A reversible capacity of ~ 98 mAh·g^{-1} and 89% capacity retention over 20 cycles were achieved. Ruan et al. prepared NaVPO$_4$F/graphene (GR) composite. It showed a decent retention of ~ 98% over 50 cycles and a reversible capacity of ~ 121 mAh·g^{-1}. [60]. The improved electrochemical performance was due to the higher Na-ion diffusivity in NaVPO$_4$F/GR compared to NaVPO$_4$F.

Recently, with regard to its high working voltage, NaVPO$_4$F has gained increasing attention. In this framework, several reports were published in the aim to boost its cycling stability and rate performances [24, 61–68]. For instance, Jin et al. designed NaVPO$_4$F/C nanofibers using electrospinning procedure (Fig. 2(a)), exhibiting a high capacity (~ 126 mAh·g^{-1} at 1 C), high rate performance (~ 61 mAh·g^{-1} at 50 C) (Fig. 2(b)), and ultralong cycle life (Fig. 2(c)) [62]. The remarkable electrochemical activity of NaVPO4F/C was due to the small nanoparticles (~ 6 nm) implanted into the porous carbon matrix, which could efficiently facilitate Na-ions diffusion kinetics. More recently, Chen et al. proposed the design of symmetric NaVPO$_4$F/C full-cell (Fig. 2(d)) [68]. The symmetric cell exhibited a reversible capacity of 83 mAh·g^{-1} at 50 mA·g^{-1}, excellent rate capability (Fig. 2(e)), and long cyclability (Fig. 2(f)). Aside from its high operating voltage, the electrochemical performances of NaVPO$_4$F cathode have been outstandingly improved, which makes it promising for high energy density sodium-ion battery technology. However, deep investigations in the Na-ion intercalation mechanism and dynamics using cutting edge *operando* techniques are highly desired.

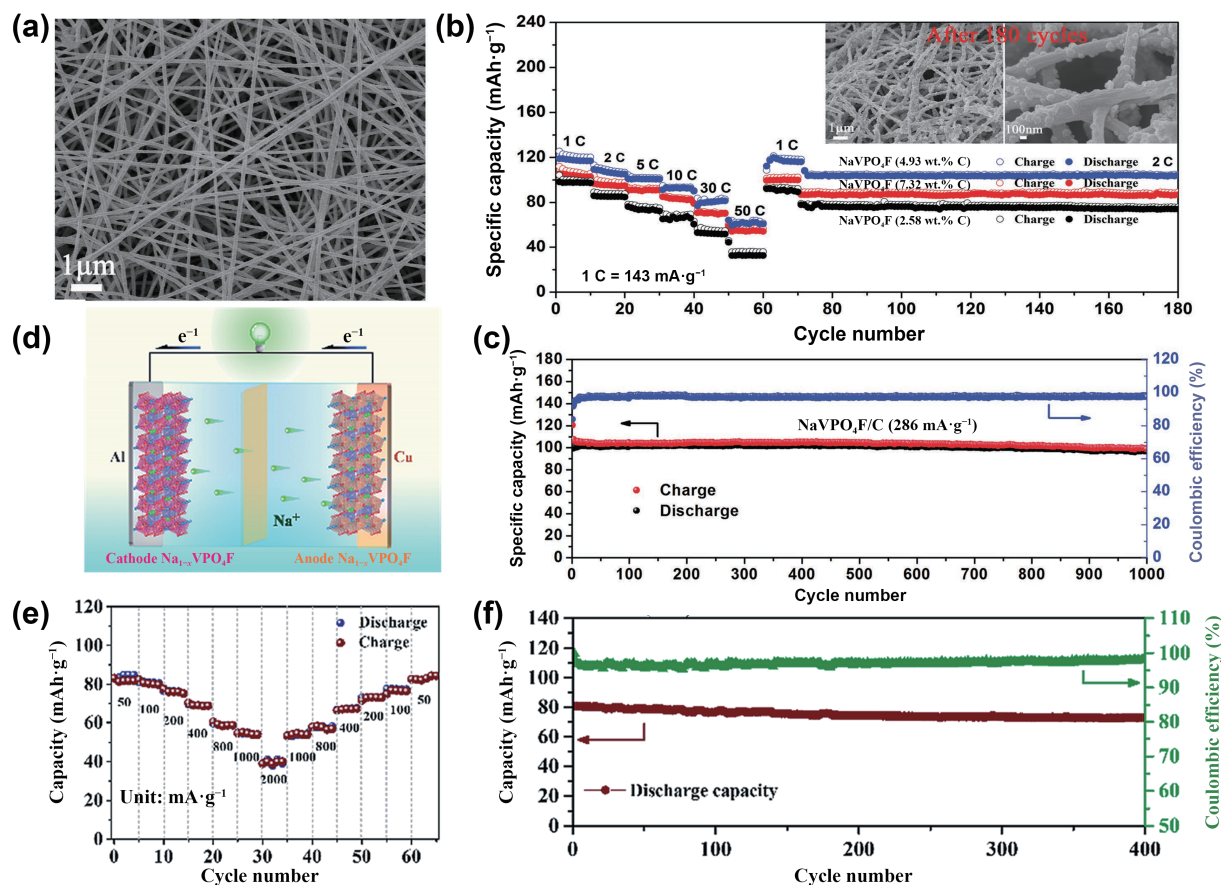**Na$_3$V$_2$(PO$_4$)$_2$F$_3$.** Le Meins et al. initially reported the

Figure 2 (a) SEM images of NaVPO$_4$F/C nanofibers. (b) Rate capability of NaVPO$_4$F/C materials (the inset is SEM analysis of NaVPO$_4$F/C after 180 cycles). (c) Cycle life 286 mA·g^{-1}. Reproduced with permission from Ref. [62], © WILEY-VCH Verlag GmbH & Co. KGaA, Weinheim 2017. (d) Design of symmetric NaVPO$_4$F/C full cells. (e) Rate capability and (f) cycle life of Na-ion full cell at 50 mA·g^{-1}. Reproduced with permission from Ref. [68], © The Royal Society of Chemistry 2019.

preparation and structural study of Na$_3$V$_2$(PO$_4$)$_2$F$_3$ [69]. They obtained in both single crystal and powder forms via solid-state and hydrothermal methods, respectively. According to Sauvage et al. [70] and Massa et al. [71], it adopted to tetragonal symmetry (P4$_2$/mnm). The crystal structure is constructed from [V^{III}$_2$O$_8$F$_3$] bi-octahedra and PO$_4$ tetrahedra. The linkage between the two octahedra is made by a bridging fluorine apex. Tetrahedra and bi-octahedra both share all eight of their oxygen vertices. This connectivity results in channels that run along the *a* and *b* axes, and their intersections form relatively substantial cavities that house Na-ions. Gover et al. firstly investigated the electrochemical Li-ion insertion into Na$_3$V$_2$(PO$_4$)$_2$F$_3$ [72]. The compound was obtained using a carbothermal reduction method. They reported a capacity of ~ 120 mAh·g^{-1}, involving the activity of two Na$^+$/f.u. at a working voltage of 4.1 V. In addition, 90% of capacity retention over 220 cycles was observed. Furthermore, Jiang et al. reported Na$_3$V$_2$(PO$_4$)$_2$F$_3$/C produced by sol–gel method [73]. They reported high capacity of 117 mAh·g^{-1} and excellent cyclability for Na$^+$ intercalation.

Reversible Na-ion intercalation into Na$_3$V$_2$(PO$_4$)$_2$F$_3$ was initially demonstrated by Shakoor et al. [74]. In addition to experimental studies, first principal calculation was conducted to elucidate the intercalation mechanism. The charge–discharge curves exposed the existence of two plateaus at 3.7 and 4.2 V$_{Na}$, giving an exceptionally high equilibrium potential of about 3.95 V$_{Na}$. A capacity of 120 mAh·g^{-1} was reached at 0.05 C. Even at 4 C, 94 mAh·g^{-1} was attained, attesting the high-rate performance. The *ex-situ* XRD analysis indicated that the Na-ion extraction/insertion operates as a single-phase reaction mechanism with very small lattice volume variation (2%).

While the crystal system of Na$_3$V$_2$(PO$_4$)$_2$F$_3$ was firstly reported adopting tetragonal (I4/mmm) symmetry, Tsirlin et al. argued that

existence of various temperature-dependent polymorphs and the RT phase was rather fitted to P4$_2$/mnm [75]. Rojo's group pointed out that Na$_3$V$_2$(PO$_4$)$_2$F$_3$ is a part of the family, Na$_3$V$_2$(PO$_4$)$_2$F$_3$–Na$_3$(VO)$_2$(PO$_4$)$_2$F, written by general chemical formula of Na$_3$V$_2$O$_{2x}$(PO$_4$)$_2$F$_{3-2x}$ (*x* is between 0 and 1) [76]. They also obtained the intermediate phase Na$_3$V$_2$O$_{2x}$(PO$_4$)$_2$F$_{3-2x}$ by hydrothermal synthesis, adopted to P4$_2$/mnm. The intermediate phase has the mixed-valence of V$^{3+/4+}$. They investigated the electrochemical mechanism using a combination of high resolution XRD (HR-XRD), X-ray absorption spectroscopy (XAS), and ^{23}Na and ^{19}F NMR [77]. On the basis of structural investigation data, they proposed the chemical formula of Na$_3$V$_2$O$_{1.6}$(PO$_4$)$_2$F$_{1.4}$. The V valence state was determined to be +3.8 for the as-prepared phase. They demonstrated that Na-ion extraction/insertion occurs as solid–solution mechanism using *ex-situ* XRD and X-ray absorption near edge structure (XANES). Furthermore, they claimed that the Na-ions extraction occurs preferentially from Na1 site.

Furthermore, Park et al. successfully synthesized the solid solution of Na$_3$(VO$_{1-x}$PO$_4$)$_2$F$_{1+2x}$ (*x* = 0.0 to 1.0) via solid-state synthesis [78]. They formed complete solid solutions over the all composition range. They exhibited a capacity of 120–130 mAh·g^{-1} and an equilibrium voltage of 3.8–3.9 V$_{Na}$.

They investigated the intercalation mechanism using both theoretical and experimental data of Na$_3$(VO$_{1-x}$PO$_4$)$_2$F$_{1+2x}$. From neutron diffraction (ND) and XRD data of chemically desodiated powder, they claimed a two-phase reaction mechanism. They also carried out theoretical calculations, showing that by triggering the 3rd Na, the voltage increases drastically above 4.5 V, which is above the stability limit of most electrolytes.

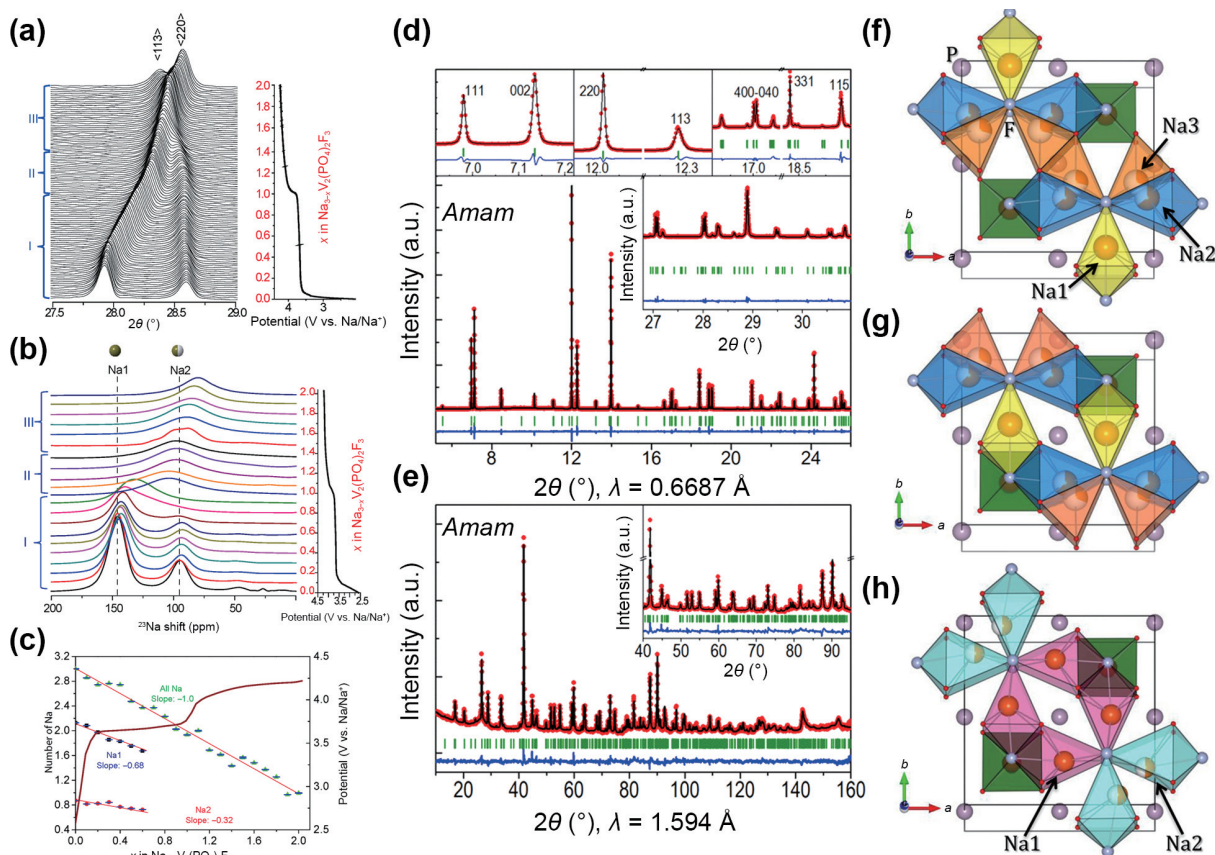Grey et al. studied the structural changes of Na$_3$V$_2$(PO$_4$)$_2$F$_3$ upon cycling process using XRD, and ^{23}Na and ^{31}P NMR [79].

Figure 3 (a) *In-situ* XRD pattern of a $Na_3V_2(PO_4)_2F_3$ electrode at different states of charge (SOC). (b) *Ex-situ* ^{23}Na NMR data of $Na_3V_2(PO_4)_2F_3$ at various SOC. (c) The occupancy of Na1 and Na2 sites during charge process calculated by integration of ^{23}Na NMR data. Reproduced with permission from Ref. [79], © American Chemical Society 2014. Rietveld refinement of (d) XRD and (e) ND patterns of $Na_3V_2(PO_4)_2F_3$ refined by the *Amam* space group. The insets reveal enlargements of relevant diffraction lines. (f) The structure representation of the result obtained from the refinement in the *Amam* space group, (g) illustrating the alternative structure with the *Amam* space group, and (h) comparison with the Na distribution reported in the literature (Le Meins et al. [69]). Reproduced with permission from Ref. [80], © American Chemical Society 2014.

They showed the existence of three phases during charging which involves different changes in electronic configurations for Na and V. *In-situ* XRD during the first charging process (Fig. 3(a)) showed a solid−solution reaction. NMR investigation (Figs. 3(b) and 3(c)) revealed that the Na extraction process is nonselective involving both Na1 and Na2 sites up to $x = 0.9$ Na. Later, Bianchini et al. demonstrated by high resolution synchrotron X-ray diffraction (SXRD) that $Na_3V_2(PO_4)_2F_3$ adopts orthorhombic system (*Amam*) which is different from well-known tetragonal system (*P4₂/mnm*) [80]. The Rietveld refined SXRD and ND patterns are depicted in Figs. 3(d) and 3(e). In the new orthorhombic system, Na atoms are distributed over three crystallographic sites rather than two sites in the tetragonal system (Figs. 3(f)–3(h)).

Bianchini et al. proposed an extremely complicated Na-ions extraction mechanism process upon charge instead of the reported simple solid−solution mechanism [81]. They carried out a detailed study of $Na_3V_2(PO_4)_2F_3$–$NaV_2(PO_4)_2F_3$ using *operando* HR-XRD. The two voltage regions around 3.7 and 4.2 V_{Na} were investigated separately (Figs. 4(a)–4(d)). The lower voltage region demonstrates three biphasic reactions that result in two phases, $Na_{2.4}V_2(PO_4)_2F_3$ and $Na_{2.2}V_2(PO_4)_2F_3$. The later composition exhibits similar structure to that of $Na_3V_2(PO_4)_2F_3$, adopting tetragonal system (*I4/mmm*) due to the presence of disorder at Na^+ sites. $Na_{2.4}V_2(PO_4)_2F_3$ instead stabilizes a long-range ordering to a d ~ 18, pointing to a superstructural arrangement. The higher voltage region is characterized by two-phase mechanism. The structure determination of the endmember, $NaV_2(PO_4)_2F_3$, was performed form the on data recorded *in-situ*, and it was solved in the *Cmc2₁* space group.

Although the structure of $Na_3V_2(PO_4)_2F_3$ was considerably studied, some of them has been inconsistent, and it has not reached the final conclusion. For better understanding the structural and electrochemical behaviors of $Na_3V_2(PO_4)_2F_3$, Broux et al. inspected the influence of oxygen concentration on the electrochemistry of $Na_3V_2(PO_4)_2F_{3−y}O_y$ ($y = 0$ to 0.5) [82]. The $Na_3V_2(PO_4)_2F_{3−y}O_y$ materials with y from 0 to 0.5 have been prepared using solid-state reaction. The results of an in-depth structural study have exposed that all the prepared compounds are isotypic and crystallize in the orthorhombic symmetry (*Amam*).

Aiming to increase the rate performance and the cyclability of $Na_3V_2(PO_4)_2F_3$, Liu et al. developed a core–shell $Na_3V_2(PO_4)_2F_3$@C material by using an *in-situ* coating procedure. An excellent capacity of 120 mAh·g⁻¹ at 1 C, a high rate performance up to 100 C, and a good cycling performance were achieved, demonstrating the exceptional electrochemical performance [83]. Moreover, high electrochemical performance was obtained when used in a full-cell configuration using $NaTi_2(PO_4)_3$@C anode, suggesting a practical applicability of $Na_3V_2(PO_4)_2F_3$@C nanocomposite for high performance SIB. More recently, Zhu et al. remarkably improved the rate performance of $Na_3V_2(PO_4)_2F_3$ via the design of ~ 30–50 nm nanoparticles associated to graphene, by employing one-step hydrothermal synthesis (Fig. 5(a)). As shown in Figs. 5(b) and 5(c), the rate capability of graphene coated NVPF (NVPF⊂GN) is considerably improved in comparison with the bare NFVP. The results showed that NVPF⊂GN material had an excellent energy density of 348 Wh·kg⁻¹ at high current density (charge/discharge within 6 min), making it a promising cathode material for SIB. It is even similar to the energy density of the well-known lithium
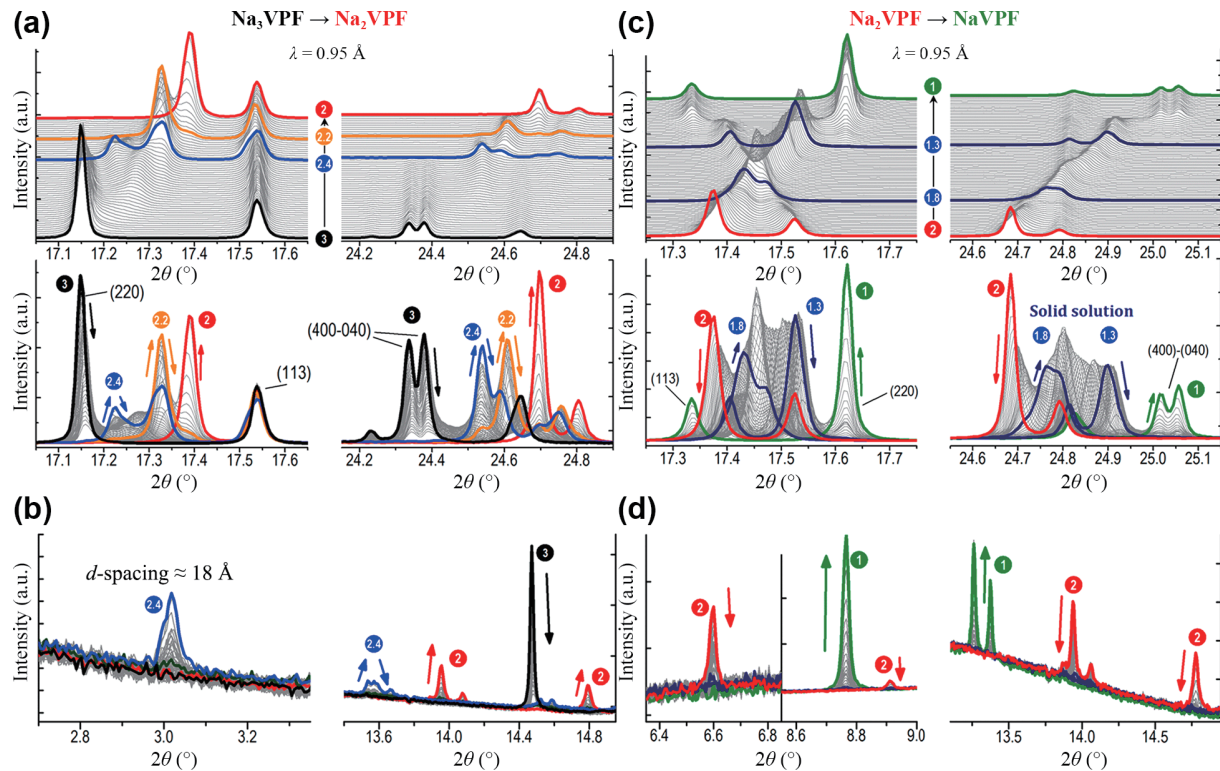
Figure 4 (a) and (b) Different compositions are formed during the bi-phase mechanism due to 1 Na$^+$ extraction from Na$_3$VPF (black pattern): The obtained compositions are Na$_{2.4}$VPF (blue pattern), Na$_{2.2}$VPF (orange pattern), and Na$_2$VPF (red pattern). (c) and (d) Synchrotron X-ray diffraction data during the extraction of 1 Na$^+$ from Na$_2$VPF (red pattern). Bi-phase mechanism is observed, causing the disappearance of Na$_2$VPF followed by a solid solution between the new compositions Na$_{1.8}$VPF and Na$_{1.3}$VPF (dark blue patterns); the green pattern represents Na$_1$VPF formed through a bi-phase mechanism. Reproduced with permission from Ref. [81], © American Chemical Society 2015.
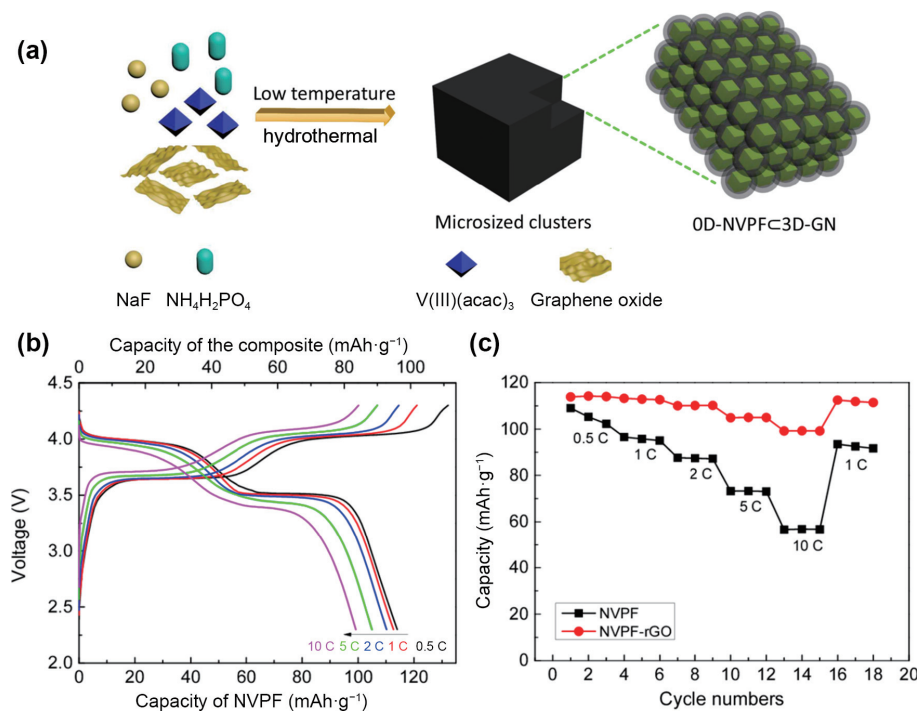

Figure 5 (a) Schematic representation of the low-temperature hydrothermal method for the preparation of NVPF⊂GN with graphene network. (b) Electrochemical profiles of NVPF⊂GN cathode material at various current rates. The upper and the lower capacity axis refer to the composite and NVPF, respectively. (c) Rate performance of NVPF and NVPF⊂GN cathode materials. Reproduced with permission from Ref. [84], © American Chemical Society 2017.

iron phosphate cathode LiFePO$_4$ [84]. In this context, i.e., enhancing the rate performance and cyclability of NVPF, several works on the developing new carbon-coated NVPF and synthesis procedures were reported [85, 86]. For instance, Zhang et al. developed an easily scalable ball milling effective method to design the sodium-rich Na$_4$V$_2$(PO$_4$)$_2$F$_3$ phase which found to crystallize

in orthorhombic system (*Amam*) [87]. They demonstrated that this method can be employed to design various types of sodium-rich materials such as polyanionic compounds, layered oxides, and alloys. The electrochemical activity of an optimized Na-rich composition, i.e., Na$_{3.5}$V$_2$(PO$_4$)$_2$F$_3$, was studied in Na-half cell. They showed a charging capacity of 167 mAh·g^{-1} which

corresponds to 24% capacity improvement and 10% rise in energy density compared with $Na_3V_2(PO_4)_2F_3$ in similar Na-half cell.

More recently, extensive research has devoted to increase the energy density by extracting 3 Na of NVPF in SIB [15, 88]. Tarascon's group electrochemically activated the 3rd Na by forming a disordered $Na_xV_2(PO_4)_2F_3$ phase in the tetragonal structure [15]. They demonstrated the possibility to electrochemically extract almost three sodium ions upon charge till 4.8 V_{Na}. It is shown in Fig. 6(a), the voltage–composition curves of various half-cell configurations using NVPF and Na metal as electrodes charged at a specific extracted sodium amount (Δx = 2.0, 2.25, 2.5, 2.75, and 3.0). Interestingly, when the electrode NVPF-3.0 was cycled between 4.4 and 1.0 V, it demonstrated an interesting capacity of 200 mAh·g^{-1}. This increase in capacity is equivalent to a 14% increase in energy density. The structural variations that occur when the third sodium is activated in NVPF were examined by *ex-situ* XRD (Figs. 6(c) and 6(d)).

The observed phase during the charging until Δx = 2 is perfectly in line with the previous literature, i.e., $Na_1V_2(PO_4)_2F_3$ can be indexed in a *Cmc2$_1$* [81]. For Δx = 3, they reported a new phase with an estimated chemical formula of $Na_0V_2(PO_4)_2F_3$ indexing to a tetragonal system (*I4/mmm*). Indeed, the authors demonstrated a new strategy to boost the energy density of $Na_3V_2(PO_4)_2F_3$ electrode material by 14%, while keeping good cycling and rate performances for advanced SIB.

More recently, Fang et al. [89] examined the impact of particle shape on Na-ion intercalation properties of $Na_3V_2(PO_4)_2F_{3-y}O_y$. They prepared a series of $Na_3V^{III}_{2-y}V^{IV}_y(PO_4)_2F_{3-y}O_y$ phosphates using solvothermal method. The XRD showed the formation of pure phases crystallizing in the *Amam* space group. Different morphologies were reported using SEM microscopy: nanosphere (NVPF1), cylindrical agglomerate (NVPF2), micrometric flake

(NVPF3), and sand-rose (NVPF4) (Fig. 7(a)). The electrochemical investigation in Na cell showed that particles morphology has an important effect on the electrochemical activity of the electrode material (Fig. 7(b)). It was shown that both cylindrical agglomerate (NVPF2) and micrometric flake (NVPF3) exhibit relatively poor electrochemical performance compared to other morphologies and it was explained by the stacking of nanosheets is perpendicular to the Na$^+$ diffusion pathways which restricted the Na$^+$ diffusion (Fig. 7(c)). Remarkably, sand-rose and nanosphere morphologies demonstrated the best electrochemical performance, especially high rate performance, which was explicated by the facile access to the Na$^+$ diffusion tunnels (Fig. 7(c)).

Newly, Essehli et al. partially substituted the vanadium by Nickel in the parent $Na_3V_2(PO_4)_2F_3$ and successfully prepared pure phase $Na_{3.2}Ni_{0.2}V_{1.8}(PO_4)_2F_2O$ (tetragonal *I4/mmm*) using a hydrothermal method [90]. This oxy-fluorophosphate was tested in both half and full cell against Na and presodiated hard carbon, respectively. In the half cell, it delivered capacity of 117 mAh·g^{-1} in the voltage window 2.5–4.5 V at 1 C current rate at room temperature, retaining 85% of initial capacity after 900 cycles. For the full cell configuration, it retained 85% of initial capacity after 500 cycles, indicating satisfactory Coulombic efficiency and cycle life. They also investigated the reaction mechanism using *in-situ* XRD in the voltage region 2–4.3 V and showed a reversible single-phase reaction.

Furthermore, an electroactive fluorophosphate $Na_5V(PO_4)_2F_2$ was firstly reported by Liang et al. in 2020 [91]. The synthesis was performed by sol–gel method and XRD showed that this material adopts two polymorphs upon synthetic temperature: the low temperature (600 °C) phase (trigonal *P3*, abbreviated as *t*-NVPF) and the high temperature (800 °C) phase (orthorhombic *Pbca*, *o*-
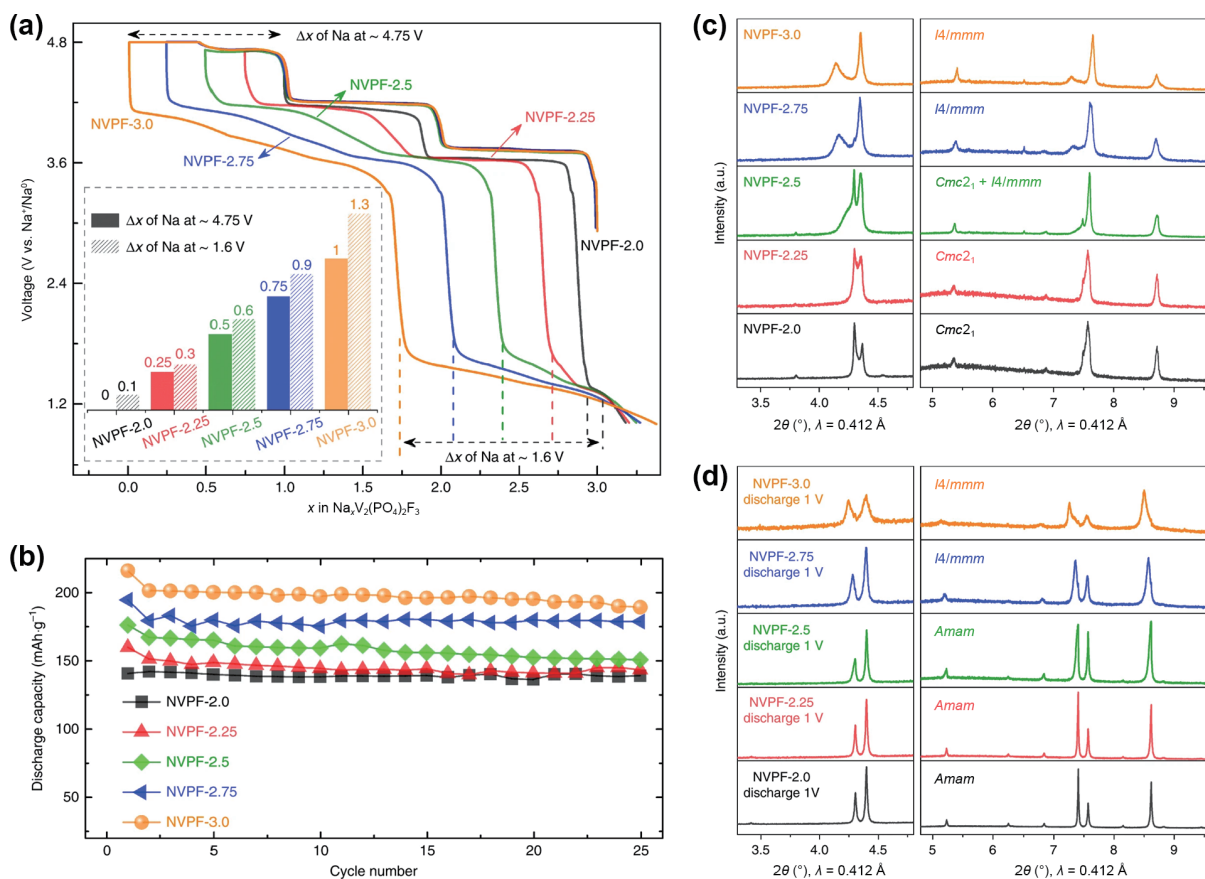

Figure 6 (a) First cycle voltage-composition profile up to 4.8 V followed by discharge to 1 V at 0.1 C rate, with controlling the amount of sodium extracted, Δx (Na) = 2.0, 2.25, 2.50, 2.75, and 3.0. The inset summarizes the Na$^+$ extracted/reinserted at in the range of 4.75–1.6 V. (b) The corresponding capacity retention plots. (c) SXRD data of NVPF electrodes. (d) SXRD data of the discharged electrodes to 1 V. Reproduced with permission from Ref. [15], © Yan, G. C. et al. 2019.
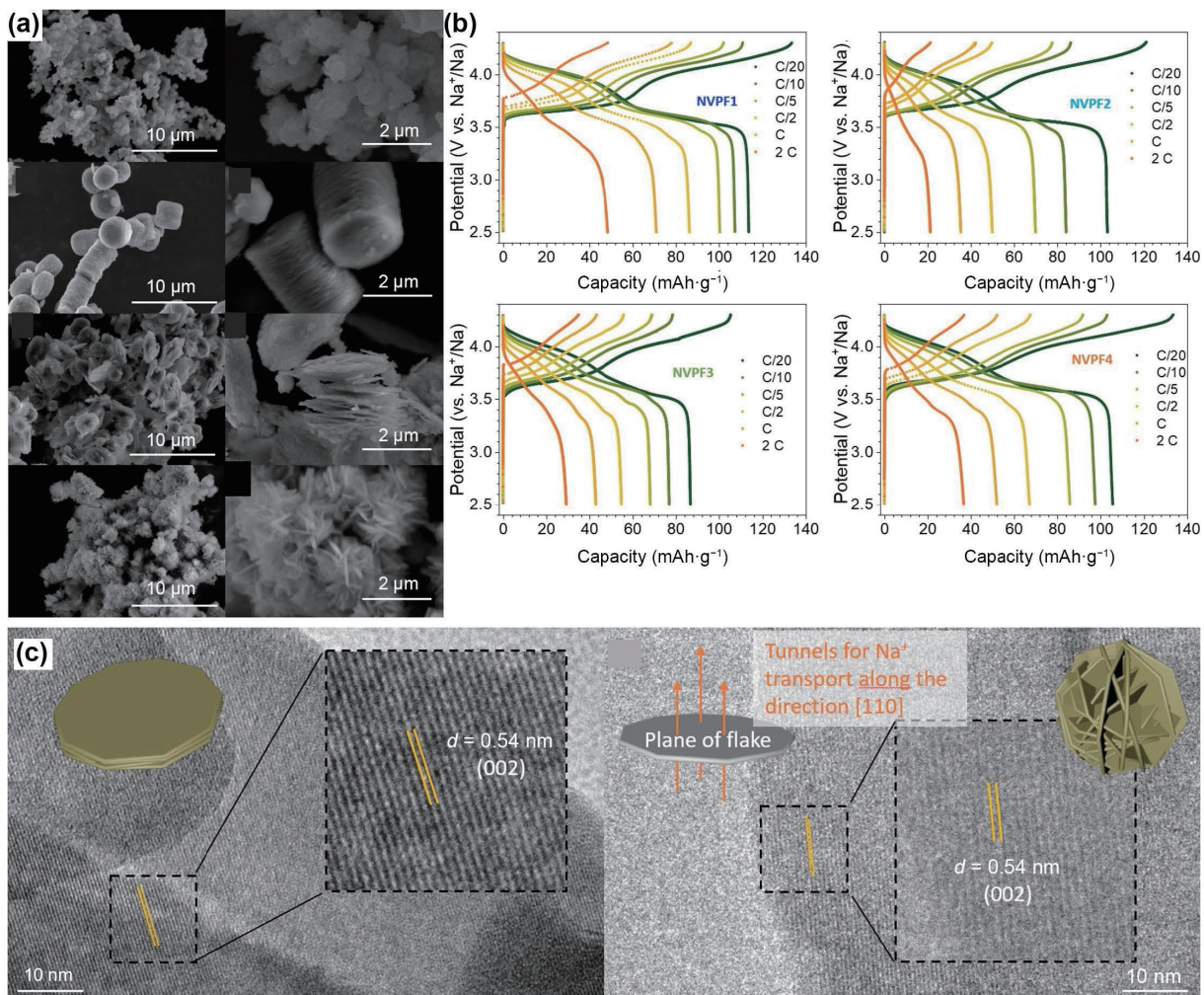
Figure 7 (a) SEM miscropraphs of the studied materials: NVPF1, NVPF2, NVPF3, and NVPF4. (b) Electrochemical profiles of NVPFO$_y$ from C/20 to 2 C. (c) TEM photographs of the NVPF3 and NVPF4 flakes with 3D models and schematics are shown in the left and right panels, respectively. Reproduced with permission from Ref. [89], © Wiley-VCH GmbH 2021.

NVPF). Both exhibit layered structures built via VO$_4$F$_2$ octahedra and PO$_4$ tetrahedra sharing corners. One Na-ions can be electrochemically extracted at 3.4 and 3.5 V$_{Na}$ for *t*-NVPF and *o*-NVPF, respectively. The authors also reported favorable rate capability and cyclability up to 1000 cycles for both polymorphs. *t*-NVPF phase slightly showed higher rate outpacing the *o*-NVPF/C phase. Furthermore, they investigated the Na extraction mechanism by *ex-situ* XRD and DFT, revealing that a two-phase was followed by a single-phase reaction mechanism upon charging. More recently, Mazumder et al. performed theoretical investigation using DFT calculations on the Na extraction from the phases Na$_5$M(PO$_4$)$_2$F$_2$ (M = Cr and V) and reported that the extraction of higher Na content (> 3 Na$^+$) requires higher voltages, and the calculated voltages were 4.77 and 4.56 V$_{Na}$ for Cr and V-based phases, respectively [92].

Indeed, high electronegative F doping is an encouraging strategy to improve the energy density of Na super ionic conductor (NASICON) cathode materials. For instance, Hou et al. introduced F substitution in Na$_4$MnV(PO$_4$)$_3$ (NMVP), creating a Na-deficient NASICON cathode, namely Na$_{3.85}$□$_{0.15}$MnV(PO$_{3.95}$F$_{0.05}$)$_3$ (NMVPF) [13]. Combining XRD and ND analyses, they confirmed the pure NASICON phase (Fig. 8(a)). ^{19}F NMR showed the F substitution of O in the crystal structure. The electrochemical investigation NMVPF in both half-cell and full-cell configurations proved high energy density of ~ 380 Wh·kg^{-1} at 0.1 C with both enhanced rate capability and cyclability outperforming the non-doped NMVP (Fig. 8(b)). A

~ 65 mAh·g^{-1} capacity at 5 C with an 85% retention after 500 cycles was achieved in full-cell configuration against a hard carbon anode, representing a significant improvement compared to Na$_4$MnV(PO$_4$)$_3$ (Fig. 8(b)). The obtained electrochemical performance was explained by the partial F substitution to O atoms within the crystal structure leading to Na vacancies, which promote Na diffusion. They also used *operando* XRD to characterize the structural evolution during the operation (Fig. 8(c)), which demonstrated a two-phase reaction mechanism with strong structural reversibility in the high voltage region, with a remarkable difference at high voltage compared to the parent phase Na$_4$MnV(PO$_4$)$_3$. Furthermore, the Na extraction/insertion process was investigated by combining refined XRD and ^{23}Na NMR (Fig. 8(d)). The results showed that the sodium extraction occurs from both Na1 and Na2 crystallographic sites, but much faster from Na2 site.

In summary, the fluorophosphates are appealing as cathode materials for SIBs. Remarkably, Na$_3$V$_2$(PO$_4$)$_2$F$_3$ is a promising candidate offering both high capacity and working voltage. It delivers 200 mAh·g^{-1} for 3 Na$^+$ per unit formula with an average voltage of 3.95 V$_{Na}$. However, the vanadium is not environmentally friendly, which limits its practical use in SIB. On the other hand, the safer cathode materials made from ecofriendly and cost-effective chemicals, for example, Na$_2$FePO$_4$F [41] and Na$_2$MnPO$_4$F [48], are promising candidates. Na$_2$FePO$_4$F [41] cathode material operates at 3.0 V$_{Na}$ with a capacity of ~ 118 mAh·g^{-1} and excellent cyclability and Coulombic efficiency.
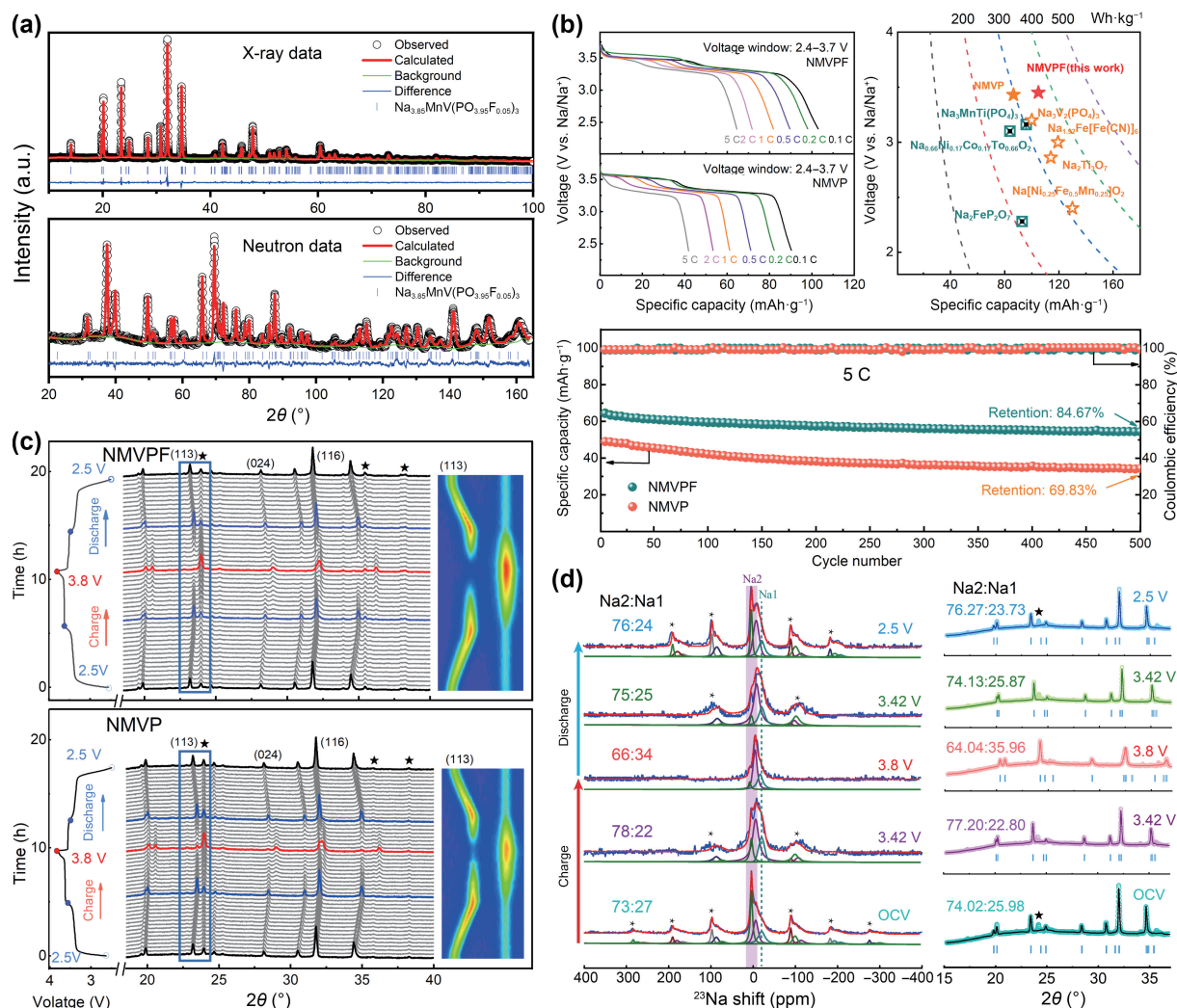
Figure 8 (a) XRD and ND pattern, and their Rietveld refinement of as-prepared NMVPF. (b) Discharge profiles for NMVPF and NMVP in full cell configuration at different C-rates (left panel), performance comparison of NMVPF with other cathodes from the literature (right panel), and full cell cycling performance (lower part). (c) *Operando* XRD data of the first cycle of NMVPF and NMVP electrodes against Na metal at 2 Na$^+$/10 h between 2.5 and 3.8 V. (d) *Ex-situ* ^{23}Na NMR spectra of NMVPF electrode. Rietveld refinement and Na quantification of selected *operando* XRD patterns of NMVPF (right panel) (★ referring to the diffraction line of Al foil or carbon). Reproduced with permission from Ref. [13], © Elsevier B.V. 2021.

Na$_2$MnPO$_4$F [48] outperforms Na$_2$FePO$_4$F in terms of energy density, offering high working voltage of 3.66 V$_{Na}$ and high capacity of ~ 121 mAh·g^{-1}, however, still suffers from poor Coulombic efficiency and cyclability. As a result, massive efforts should be made in the near future to optimize Na$_2$MnPO$_4$F performance by particle size engineering and carbon coating in order to meet the cathode requirements for high energy density SIB applications.

3 Fluorosulfates: NaFeSO$_4$F

Sulfate chemistry has grown in popularity for the progress of novel high-voltage electrode materials for LIB and SIB. The secret behind the increasing attention about sulfates is the high electronegativity of SO$_4^{2-}$ polyanion which outpaces phosphates, and for further increasing the inductive effect, research has been oriented to the fluorosulphate chemistry.

Since the report of the electrochemical activity of tavorite LiFeSO$_4$F in 2009 by Recham et al. [27], Tarascon's group and Nazar's group extensively investigated the NaFeSO$_4$F [93–95]. This fluorosulfate can be produced by several approaches such as solid-state reaction [93], ionothermal synthesis method [93], polyol-assisted synthesis [94], and also by dehydration of NaFeSO$_4$F·2H$_2$O [96, 97]. NaFeSO$_4$F adopts tavorite-like structure (maxwellite-type structure) with monoclinic structcure (*C2/c*). Its

crystal framework is built up from corner-sharing of FeO$_4$F$_2$ octahedra linked to SO$_4$ tetrahedra producing tunnels where the Na ions can be stored [97].

The electrochemical activity of NaFeSO$_4$F in SIB was firstly demonstrated by Tarascon's group [93, 98]. They reported the electrochemical extraction of 0.7 Na from the structure relying on the Fe$^{II/III}$ redox couple at around 3.5 V$_{Na}$. While NaFeSO$_4$F exhibits high operating voltage, it shows poor electrochemical activity compared to the Li-rich tavorite LiFeSO$_4$F counterpart. Moreover, Kim et al. reported a new polymorph of NaFeSO$_4$F which crystallizes in triplite-type structure exhibiting high operating voltage of 3.7 V$_{Na}$ and improved electrochemical performances than the tavorite polymorph (Fig. 9(a)) [23]. The triplite NaFeSO$_4$F delivered almost theoretical capacity (~ 138 mAh·g^{-1}) at 0.01 C rate. The origin of the enhanced electrochemical performance of triplite NaFeSO$_4$F compared to the tavorite was explained by the difference in fluorine position in the FeO$_4$F$_2$ octahedra, i.e., triplite's cis fluorine position as compared to tavorite's trans fluorine position, which may affect thermodynamics. The authors claimed that the F atoms significantly closer to one another in the cis configuration which can increase the electronegativity in the triplite phase (Fig. 9(a)), and a lower volume change during desodiation ($\Delta V/V = 6.9\%$) was also reported. In this context, Momida et al. performed first-
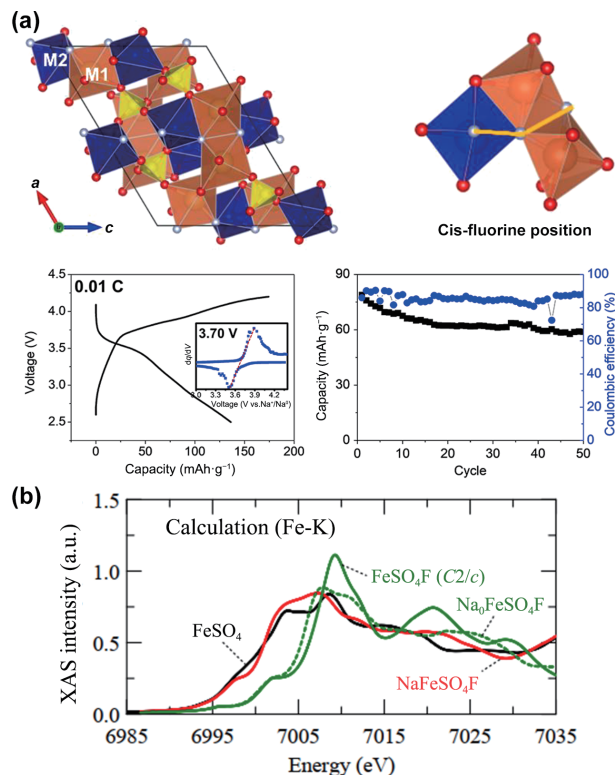
Figure 9 (a) Illustration of the crystal structure of triplite NaFeSO₄ (top part) and charge discharge curve at a rate of 0.01 C and cycling performance at 0.1 C of triplite $NaFeSO_4F$ (lower part). Reproduced with permission from Ref. [23], © American Chemical Society 2018. (b) $FeSO_4$ (black), $NaFeSO_4F$ (red), and $FeSO_4F$ (green) XAS near Fe K-edge spectra simulated by GGA+*U*. The green line is the simulated $FeSO_4F$ spectrum from the *C2/c* structural model, while the green dotted line represents the Na derived $NaFeSO_4F$ spectrum. Reproduced with permission from Ref. [99], © The Physical Society of Japan 2019.

principles investigation of $NaFeSO_4F$ as cathode in SIB [99]. They studied spectroscopic and electronic properties of $NaFeSO_4F$ using generalized gradient approximation (GGA)+*U* calculations and they calculated an estimated working voltage of 3.08 V_{Na}. They also computed XAS at Fe, Na, and F K-edges for $FeSO_4F$ and $NaFeSO_4F$ end members, respectively. Interestingly, comparing the discharged to the charged state, Fe K-edge showed an important displacement of the absorption threshold and the near edge peak position, which was explained by the oxidation of Fe^{2+} in $NaFeSO_4F$ to Fe^{3+} in $FeSO_4$ (Fig. 9(b)). This kind of study provides useful structural insights that can help in understanding the mechanistic reactions in $NaFeSO_4F$ cathode material. Furthermore, the $NaMSO_4F$ family (M = Mg, Co, Cu, and Zn) was successfully synthesized using solid-state reactions by Tarascon's group [93, 97]. They adopted the maxwellite-type structure (tavorite-like framework) with monoclinic system (*C2/c*). However, the study showed no electrochemical activity versus Na^+/Na.

The exploration of other alkali metals brought to light K-based fluorosulphates, $KMSO_4F$ (M = Fe, Co, and Ni) [100]. These fluorosulphates were deployed by solid-state reaction, and pure phases were formed at 380 °C for Fe-based phase and at 290 °C for both Co- and Ni-based phases. They crystallized in orthorhombic system (*Pna*2₁). Their structure is constructed from the linkage of MO_4F_2 octahedra through their vertices via F atoms leading to zigzag chains. Each two neighboring MO_4F_2 octahedra are bridged by two SO_4 tetrahedra. As illustrated in Figs. 10(a) and 10(b), the linking of these chains produces two types of large tunnels running along *a*- and *b*-axis where K^+ can be located. The authors investigated by *in-situ* XRD the oxidation of $KFeSO_4F$ using NO_2BF_4 dissolved in acetonitrile to reveal the structural

information for the $FeSO_4F$ end member. The results showed that $FeSO_4F$ is isostructural to $KTiOPO_4$ (KTP) with *Pnna* space group. The electrochemical activity was investigated for Fe-based phase in Li, Na, and K-ions batteries (Fig. 10(c)). The results showed reversible activity of ~ 0.9 Li^+ per formula unit around ~ 3.7 V_{Li} for a few cycles at C/20 rate. For Na- and K-ion batteries, a reversible uptake of 0.85 Na^+ and 0.8 K^+ ions per formula unit was reported. The authors observed low polarization in case of Na-ion battery, which was explained by high Na diffusion kinetics compared to Li and K counterparts. For the electrochemical investigation of Ni and Co-based $KMSO_4F$ phases versus Li, they reported that some K can be extracted from the Co phase at high working voltage of ~ 4.9 V with large irreversibility due to electrolyte decomposition, whereas no electrochemical activity was observed for the Ni phase even at 5.2 V. Furthermore, another low temperature polymorph of $KFeSO_4F$ was reported by Lander et al. [101], which was synthesized by solid-state reaction at relatively low temperature at 310 °C. It crystallizes in monoclinic symmetry (*C2/c*). Its crystal framework is complex layered-structure built up from FeO_4F_2 octahedra and SO_4 groups where K^+ located in the inter-layer spaces. These reports confirm the structural diversity and polymorphism of fluorosulphate family.

In summary, fluorosulfates are promising new cathode materials that have attracted recently several research groups because of their outstanding high working voltages. For instance, the low-cost triplite $NaFeSO_4F$ shows promising crystal framework with tunnels allowing high Na conduction. It can be produced using various techniques such as solid-state, ionothermal, and polyol-assisted methods. It operates at 3.7 V_{Na} with a capacity of 138 mAh·g⁻¹, while Coulombic efficiency and cycling performance possibly will be improved using conventional methods such as carbon-coating and particle size/morphology optimization. Furthermore, the structural data base of fluorosulfates is still limited, making it a suitable playground for investigating novel low-cost materials such as Mn and Ni-based systems using various synthesis procedures such as hydrothermal and sol–gel. Despite the fact that Co and V-based materials have a high working voltage, concerns regarding their high cost and toxicity have hindered their practical deployment in batteries. Besides, exploring other mixed polyanions phosphate-sulfate can be a promising strategy to design new cathode materials with interesting structural and electrochemical properties.

4 Summary and perspectives

In the current review, we debated recent advancements in the progress of high energy density cathodes based on fluorophosphates and fluorosulfates for SIB. Among many candidates, polyanionic materials are highly attractive choice because they shows high operating potential and stable cyclability due to stable crystal frameworks and high inductive effect of polyanions. The most attractive cathode material for SIBs offering both high capacity and working voltage is $Na_3V_2(PO_4)_2F_3$. As summarized in Table 1 and Fig. 11, $Na_3V_2(PO_4)_2F_3$ material delivers 200 mAh·g⁻¹ for 3 Na⁺ per unit formula with a working voltage of 3.95 V_{Na}. However, the toxicity of V hinders its practical use in SIB. The safer cathode materials made from ecofriendly and cost-effective chemicals, e.g., Na_2FePO_4F [41] and Na_2MnPO_4F [48], are promising candidates. Na_2FePO_4F [41] cathode material operates at 3.0 V_{Na} with a capacity of ~ 118 mAh·g⁻¹ and excellent cyclability. Na_2MnPO_4F [48] outperforms Na_2FePO_4F in terms of energy density offering high working voltage of 3.66 V_{Na} and high capacity of ~ 121 mAh·g⁻¹, however, still suffers from poor cycling performance. Therefore, enormous efforts should be spent in near future for optimizing Na_2MnPO_4F performance via particle size engineering and carbon coating to fulfil the cathode requirements for high energy density SIB applications.
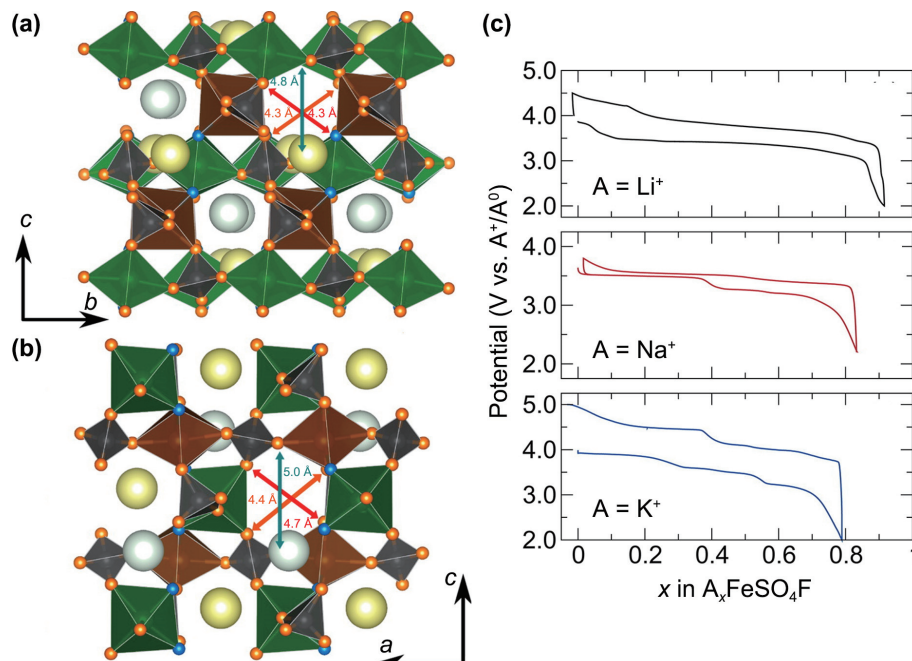
Figure 10 An illustration showing the $KMSO_4F$ crystal structure in (a) *a* direction and (b) *b* direction. The atoms represented here are M1 (green), M2 (brown), O (orange), S (dark gray), K1 (yellow), K2 (gray), and F (blue). (c) K_0FeSO_4F charge–discharge curves, which were produced by electrochemically oxidizing $KFeSO_4F$ in a $Li/KFeSO_4F$ cell. The obtained $FeSO_4F$ was cycled vs. Li, Na, and K metals using 1 M $AClO_4$ (A = Li, Na, and K) in PC at C/20. Reproduced with permission from Ref. [100], © American Chemical Society 2012.
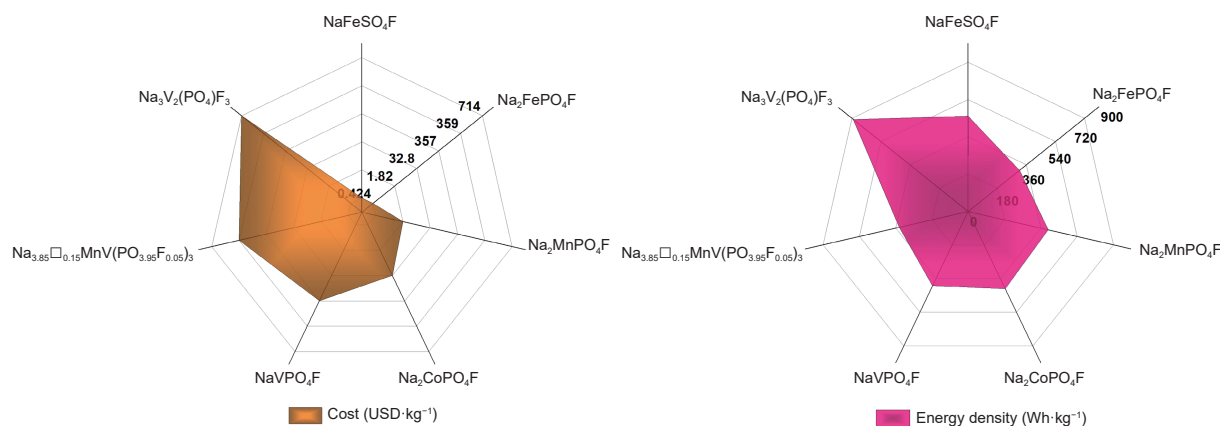

Figure 11 Radar plot comparison of (left plot) cost (USD·kg⁻¹) of the transition metal in each cathode material and (right plot) the calculated energy density of the cathode materials gathered in Table 1.

Table 1 Overview of relevant fluorophosphates and fluorosulfates cathode materials for SIBs

Materials	Average voltage (V_{Na})	Theoretical capacity (mAh·g⁻¹) per Na^+	Specific capacity (mAh·g⁻¹)	Theoretical energy density (Wh·Kg⁻¹) per Na^+	Coulombic efficiency/ cycle life
Fluorophosphates					
Na_2FePO_4F [41]	3.00	124.20	117.8 (0.1 C)	372.58	85%/2000 cycles at 5 C
Na_2MnPO_4F [48]	3.66	124.73	120.7 (10 mA·g⁻¹)	456.50	70%/30 cycles at 10 mA·g⁻¹
Na_2CoPO_4F [53]	4.30	122.45	107.0 (61 mA·g⁻¹)	526.52	37%/20 cycles at 61 mA·g⁻¹
$NaVPO_4F$ [62]	3.50	142.64	126.3 (1 C)	499.22	96.5%/1000 cycles at 2 C
$Na_3V_2(PO_4)_2F_3$ [15]	3.95	64.15	200.0 (0.1 C)	253.39	—/25 cycles at 0.1 C
$Na_{3.85}\square_{0.15}MnV(PO_{3.95}F_{0.05})_3$ [13]	3.50	55.87	110.0 (0.1 C)	195.52	84.6%/500 cycles at 5 C
Fluorosulfates					
Triplite $NaFeSO_4F$ [23]	3.70	138.23	138.0 (0.01 C)	511.45	64%/50 cycles at 0.1 C

Fluorosulfates represent a new category of cathode materials that have attracted recently several research groups because of their promising high working voltages. For instance, the low-cost triplite $NaFeSO_4F$ operates at 3.7 V_{Na} with a capacity of 138 mAh·g⁻¹, though the Coulombic efficiency and cycling performance still need improvement by the usual approaches such as carbon-coating and particle size/morphology optimizing. Furthermore, the structural data base of fluorosulfates is still poor, therefore it is a promising playground for exploring new low-cost materials such as Mn- and Ni-based systems. Even though Co-

and V-based materials offer high operating voltage, the concern about their high cost and toxicity has complicated their practical application in batteries.

To design high energy density cathode materials, researchers should explore new materials with open frameworks such as layered-type structures or structures with tunnels/cavities, large enough to facilitate the Na-extraction from the crystal framework. The crystal framework can be constructed from phosphate groups and/or sulfate groups in addition to transition metals. Sulfates exhibit higher operating voltage; however, they suffer from poor thermal stability, unlike phosphates which show excellent thermal stability. To innovate new cathodes with both high working voltage and high thermal stability, fluorophosphates can be a better choice. The transition metals should be carefully selected, considering their cost and their toxicity to the environment. For instance, iron, manganese, titanium, and nickel are suitable low-cost and ecofriendly candidates. To achieve this goal, materials chemists should develop and optimize low-cost synthesis procedures such as sol–gel and pechini methods to prepare *in-situ* carbon coated materials with suitable particle size and morphology in order to boost the electrochemical performances including rate capability, Coulombic efficiency, and cycle life. Subsequently, an in-depth structural study should be performed using cutting edge characterizations such as single crystal XRD, X-ray photoelectron spectroscopy (XPS), XAS, and NMR to understand the structure which plays a paramount important role for the materials properties. The structural understanding upon battery cycling via *operando* techniques (XRD, NMR, and XAS) is also highly desirable to highlight the intercalation mechanism of the studied materials.

Acknowledgements

References

[1] Li, B. B.; Gao, X. F.; Li, J. Y.; Yuan, C. Life cycle environmental impact of high-capacity lithium ion battery with silicon nanowires anode for electric vehicles. *Environ. Sci. Technol.* **2014**, *48*, 3047–3055.

[2] Dunn, B.; Kamath, H.; Tarascon, J. M. Electrical energy storage for the grid: A battery of choices. *Science* **2011**, *334*, 928–935.

[3] Zubi, G.; Dufo-López, R.; Carvalho, M.; Pasaoglu, G. The lithium-ion battery: State of the art and future perspectives. *Renew. Sustain. Energy Rev.* **2018**, *89*, 292–308.

[4] Scrosati, B.; Hassoun, J.; Sun, Y. K. Lithium-ion batteries. A look into the future. *Energy Environ. Sci.* **2011**, *4*, 3287–3295.

[5] Tarascon, J. M. Is lithium the new gold. *Nat. Chem.* **2010**, *2*, 510–510.

[6] Pan, H. L.; Hu, Y. S.; Chen, L. Q. Room-temperature stationary sodium-ion batteries for large-scale electric energy storage. *Energy Environ. Sci.* **2013**, *6*, 2338–2360.

[7] Bauer, A.; Song, J.; Vail, S.; Pan, W.; Barker, J.; Lu, Y. H. The scale-up and commercialization of nonaqueous Na-ion battery technologies. *Adv. Energy Mater.* **2018**, *8*, 1702869.

[8] Ren, M.; Fang, H. Y.; Wang, C. C.; Li, H. X.; Li, F. J. Advances on manganese-oxide-based cathodes for Na-ion batteries. *Energy Fuels* **2020**, *34*, 13412–13426.

[9] Goikolea, E.; Palomares, V.; Wang, S. J.; de Larramendi, I. R.; Guo, X.; Wang, G. X.; Rojo, T. Na-ion batteries-approaching old and new challenges. *Adv. Energy Mater.* **2020**, *10*, 2002055.

[10] Zhang, L. P.; Wang, W.; Lu, S. f.; Xiang, Y. Carbon anode materials: A detailed comparison between Na-ion and K-ion batteries. *Adv. Energy Mater.* **2021**, *11*, 2003640.

[11] Hu, Y. S.; Li, Y. Q. Unlocking sustainable Na-ion batteries into industry. *ACS Energy Lett.* **2021**, *6*, 4115–4117.

[12] Chayambuka, K.; Mulder, G.; Danilov, D. L.; Notten, P. H. From Li-ion batteries toward Na-ion chemistries: Challenges and opportunities. *Adv. Energy Mater.* **2020**, *10*, 2001310.

[13] Hou, J. R.; Hadouchi, M.; Sui, L.; Liu, J.; Tang, M. X.; Kan, W. H.; Avdeev, M.; Zhong, G. M.; Liao, Y. K.; Lai, Y. H. et al. Unlocking fast and reversible sodium intercalation in NASICON Na$_4$MnV(PO4)$_3$ by fluorine substitution. *Energy Storage Mater.* **2021**, *42*, 307–316.

[14] Hadouchi, M.; Yaqoob, N.; Kaghazchi, P.; Tang, M. X.; Liu, J.; Sang, P. F.; Fu, Y. Z.; Huang, Y. H.; Ma, J. W. Fast sodium intercalation in Na$_{3.41}$£$_{0.59}$FeV(PO4)$_3$: A novel sodium-deficient NASICON cathode for sodium-ion batteries. *Energy Storage Mater.* **2021**, *35*, 192–202.

[15] Yan, G. C.; Mariyappan, S.; Rousse, G.; Jacquet, Q.; Deschamps, M.; David, R.; Mirvaux, B.; Freeland, J. W.; Tarascon, J. M. Higher energy and safer sodium ion batteries via an electrochemically made disordered Na$_3$V$_2$(PO$_4$)$_2$F$_3$ material. *Nat. Commun.* **2019**, *10*, 585.

[16] Vaalma, C.; Buchholz, D.; Weil, M.; Passerini, S. A cost and resource analysis of sodium-ion batteries. *Nat. Rev. Mater.* **2018**, *3*, 18013.

[17] Li, W. J.; Han, C.; Wang, W. L.; Gebert, F.; Chou, S. L.; Liu, H. K.; Zhang, X. H.; Dou, S. X. Commercial prospects of existing cathode materials for sodium ion storage. *Adv. Energy Mater.* **2017**, *7*, 1700274.

[18] Li, H. X.; Xu, M.; Zhang, Z. A.; Lai, Y. Q.; Ma, J. M. Engineering of polyanion type cathode materials for sodium-ion batteries: Toward higher energy/power density. *Adv. Funct. Mater.* **2020**, *30*, 2000473.

[19] Barpanda, P.; Nishimura, S. I.; Yamada, A. High-voltage pyrophosphate cathodes. *Adv. Energy Mater.* **2012**, *2*, 841–859.

[20] Ni, Q.; Bai, Y.; Wu, F.; Wu, C. Polyanion-type electrode materials for sodium-ion batteries. *Adv. Sci.* **2017**, *4*, 1600275.

[21] Li, H. X.; Jin, T.; Chen, X. B.; Lai, Y. Q.; Zhang, Z. A.; Bao, W. Z.; Jiao, L. F. Rational architecture design enables superior Na storage in greener NASICON-Na$_4$MnV(PO4)$_3$ cathode. *Adv. Energy Mater.* **2018**, *8*, 1801418.

[22] Manthiram, A.; Goodenough, J. B. Lithium-based polyanion oxide cathodes. *Nat. Energy* **2021**, *6*, 844–845.

[23] Kim, M.; Kim, D.; Lee, W.; Jang, H. M.; Kang, B. New class of 3.7 V Fe-based positive electrode materials for Na-ion battery based on cation-disordered polyanion framework. *Chem. Mater.* **2018**, *30*, 6346–6352.

[24] Law, M.; Balaya, P. NaVPO$_4$F with high cycling stability as a promising cathode for sodium-ion battery. *Energy Storage Mater.* **2018**, *10*, 102–113.

[25] Barpanda, P.; Ati, M.; Melot, B. C.; Rousse, G.; Chotard, J. N.; Doublet, M. L.; Sougrati, M. T.; Corr, S. A.; Jumas, J. C.; Tarascon, J. M. A 3.90 V iron-based fluorosulphate material for lithium-ion batteries crystallizing in the triplite structure. *Nat. Mater.* **2011**, *10*, 772–779.

[26] Barpanda, P.; Oyama, G.; Nishimura, S. I.; Chung, S. C.; Yamada, A. A 3.8-V earth-abundant sodium battery electrode. *Nat. Commun.* **2014**, *5*, 4358.

[27] Recham, N.; Chotard, J. N.; Dupont, L.; Delacourt, C.; Walker, W.; Armand, M.; Tarascon, J. M. A 3.6 V lithium-based fluorosulphate insertion positive electrode for lithium-ion batteries. *Nat. Mater.* **2010**, *9*, 68–74.

[28] Wang, J. J.; Kang, J. Z.; Gu, Z. Y.; Liang, Q. H.; Zhao, X. Y.; Wang, X. M.; Guo, R. S.; Yu, H.; Du, C. F.; Wu, X. L. Localized electron density redistribution in fluorophosphate cathode: Dangling anion regulation and enhanced Na-ion diffusivity for sodium-ion batteries. *Adv. Funct. Mater.* **2022**, *32*, 2109694.

[29] Morais, W. G.; Leite, M. M.; Torresi, R. M. Titanium- and niobium-doped fluorophosphates as positive electrodes for sodium-ion batteries. *J. Electroanal. Chem.* **2021**, *897*, 115595.

[30] Gu, Z. Y.; Guo, J. Z.; Sun, Z. H.; Zhao, X. X.; Wang, X. T.; Liang, H. J.; Zhao, B.; Li, W. H.; Pan, X. M.; Wu, X. L. Aliovalent-ion-induced lattice regulation based on charge balance theory: Advanced fluorophosphate cathode for sodium-ion full batteries. *Small* **2021**, *17*, 2102010.

[31] Chang, W.; Zhang, X. Y.; Qu, J.; Chen, Z.; Zhang, Y. J.; Sui, Y.;

Ma, X. F.; Yu, Z. Z. Freestanding Na$_3$V$_2$O$_2$(PO$_4$)$_2$F/graphene aerogels as high-performance cathodes of sodium-ion full batteries. *ACS Appl. Mater. Interfaces* **2020**, *12*, 41419–41428.

[32] Zheng, L. M.; Zhang, D. T.; Wang, X. Y.; Guo, G. S. Continuous-flow rapid and controllable microfluidic synthesis of sodium vanadium fluorophosphate as a cathode material. *Appl. Mater. Today* **2021**, *23*, 101032.

[33] Ellis, B. L.; Makahnouk, W. R. M.; Makimura, Y.; Toghill, K.; Nazar, L. F. A multifunctional 3.5 V iron-based phosphate cathode for rechargeable batteries. *Nat. Mater.* **2007**, *6*, 749–753.

[34] Ellis, B. L.; Michael Makahnouk, W. R.; Rowan-Weetaluktuk, W. N.; Ryan, D. H.; Nazar, L. F. Crystal structure and electrochemical properties of A$_2$MPO$_4$F fluorophosphates (A = Na, Li; M = Fe, Mn, Co, Ni). *Chem. Mater.* **2010**, *22*, 1059–1070.

[35] Kabalov, Y. K.; Simonov, M. A.; Belov, N. V. Crystalline structure of basic iron ortho-phosphate, Na$_2$FePO$_4$(OH). *Dokl. Akad. Nauk SSSR* **1974**, *215*, 850–853.

[36] Sanz, F.; Parada, C.; Ruíz-Valero, C. Crystal growth, crystal structure and magnetic properties of disodium cobalt fluorophosphate. *J. Mater. Chem.* **2001**, *11*, 208–211.

[37] Kawabe, Y.; Yabuuchi, N.; Kajiyama, M.; Fukuhara, N.; Inamasu, T.; Okuyama, R.; Nakai, I.; Komaba, S. Synthesis and electrode performance of carbon coated Na$_2$FePO$_4$F for rechargeable Na batteries. *Electrochem. Commun.* **2011**, *13*, 1225–1228.

[38] Ling, R.; Cai, S.; Shen, S. B.; Hu, X. D.; Xie, D. L.; Zhang, F. Y.; Sun, X. H.; Yu, N.; Wang, F. W. Synthesis of carbon coated Na$_2$FePO$_4$F as cathode materials for high-performance sodium ion batteries. *J. Alloys Compd.* **2017**, *704*, 631–640.

[39] Deng, X.; Shi, W. X.; Sunarso, J.; Liu, M. L.; Shao, Z. P. A green route to a Na$_2$FePO$_4$F-based cathode for sodium ion batteries of high rate and long cycling life. *ACS Appl. Mater. Interfaces* **2017**, *9*, 16280–16287.

[40] Ko, W.; Yoo, J. K.; Park, H.; Lee, Y.; Kim, H.; Oh, Y.; Myung, S. T.; Kim, J. Development of Na$_2$FePO$_4$F/conducting-polymer composite as an exceptionally high performance cathode material for Na-ion batteries. *J. Power Sources* **2019**, *432*, 1–7.

[41] Wang, F. F.; Zhang, N.; Zhao, X. D.; Wang, L. X.; Zhang, J.; Wang, T. S.; Liu, F. F.; Liu, Y. C.; Fan, L. Z. Realizing a high-performance Na-storage cathode by tailoring ultrasmall Na$_2$FePO$_4$F nanoparticles with facilitated reaction kinetics. *Adv. Sci.* **2019**, *6*, 1900649.

[42] Langrock, A.; Xu, Y. H.; Liu, Y. H.; Ehrman, S.; Manivannan, A.; Wang, C. S. Carbon coated hollow Na$_2$FePO$_4$F spheres for Na-ion battery cathodes. *J. Power Sources* **2013**, *223*, 62–67.

[43] Yan, J. H.; Liu, X. B.; Li, B. Y. Nano-assembled Na$_2$FePO$_4$F/carbon nanotube multi-layered cathodes for Na-ion batteries. *Electrochem. Commun.* **2015**, *56*, 46–50.

[44] Smiley, D. L.; Goward, G. R. *Ex situ* ^{23}Na solid-state NMR reveals the local Na-ion distribution in carbon-coated Na$_2$FePO$_4$F during electrochemical cycling. *Chem. Mater.* **2016**, *28*, 7654–7656.

[45] Li, Q.; Liu, Z. G.; Zheng, F.; Liu, R.; Lee, J.; Xu, G. L.; Zhong, G. M.; Hou, X.; Fu, R. Q.; Chen, Z. H. et al. Identifying the structural evolution of the sodium ion battery Na$_2$FePO$_4$F Cathode. *Angew. Chem.* **2018**, *130*, 12094–12099.

[46] Yakubovich, O. V.; Karimova, O. V.; Mel'nikov, O. K. The mixed anionic framework in the structure of Na$_2$\{MnF[PO$_4$]\}. *Acta Cryst.* **1997**, *53*, 395–397.

[47] Recham, N.; Chotard, J. N.; Dupont, L.; Djellab, K.; Armand, M.; Tarascon, J. M. Ionothermal synthesis of sodium-based fluorophosphate cathode materials. *J. Electrochem. Soc.* **2009**, *156*, A993.

[48] Zhong, Y. J.; Wu, Z. G.; Tang, Y.; Xiang, W.; Guo, X. D.; Zhong, B. H. Micro-nano structure Na$_2$MnPO$_4$F/C as cathode material with excellent sodium storage properties. *Mater. Lett.* **2015**, *145*, 269–272.

[49] Wu, L.; Hu, Y.; Zhang, X. P.; Liu, J. Q.; Zhu, X.; Zhong, S. K. Synthesis of carbon-coated Na$_2$MnPO$_4$F hollow spheres as a potential cathode material for Na-ion batteries. *J. Power Sources* **2018**, *374*, 40–47.

[50] Hu, Y.; Wu, L.; Liao, G. X.; Yang, Y.; Ye, F.; Chen, J. B.; Zhu, X.; Zhong, S. K. Electrospinning synthesis of Na$_2$MnPO$_4$F/C

nanofibers as a high voltage cathode material for Na-ion batteries. *Ceram. Int.* **2018**, *44*, 17577–17584.

[51] Ling, R.; Cai, S.; Shen, K. E.; Sang, Z. Y.; Xie, D. L.; Sun, J. Y.; Xiong, K. Z.; Guo, J. Z.; Sun, X. H. Dual carbon-confined Na$_2$MnPO$_4$F nanoparticles as a superior cathode for rechargeable sodium-ion battery. *Ceram. Int.* **2019**, *45*, 19799–19807.

[52] Kubota, K.; Yokoh, K.; Yabuuchi, N.; Komaba, S. Na$_2$CoPO$_4$F as a high-voltage electrode material for Na-ion batteries. *Electrochemistry* **2014**, *82*, 909–911.

[53] Zou, H.; Li, S.; Wu, X.; McDonald, M. J.; Yang, Y. Spray-drying synthesis of pure Na$_2$CoPO$_4$F as cathode material for sodium ion batteries. *ECS Electrochem. Lett.* **2015**, *4*, A53–A55.

[54] Barker, J.; Saidi, M. Y.; Swoyer, J. L. A sodium-ion cell based on the fluorophosphate compound NaVPO$_4$ F. *Electrochem. Solid-State Lett.* **2003**, *6*, A1.

[55] Barker, J.; Saidi, M. Y.; Swoyer, J. L. A comparative investigation of the Li insertion properties of the novel fluorophosphate phases, NaVPO$_4$F and LiVPO$_4$F. *J. Electrochem. Soc.* **2004**, *151*, A1670.

[56] Zhuo, H. T.; Wang, X. Y.; Tang, A. P.; Liu, Z. M.; Gamboa, S.; Sebastian, P. J. The preparation of NaV$_{1-x}$Cr$_x$PO$_4$F cathode materials for sodium-ion battery. *J. Power Sources* **2006**, *160*, 698–703.

[57] Liu, Z. M.; WANG, X. Y.; Wang, Y.; Tang, A. P.; Yang, S. Y.; He, L. F. Preparation of NaV$_{1-x}$Al$_x$PO$_4$F cathode materials for application of sodium-ion battery. *Trans. Nonferrous Met. Soc. China* **2008**, *18*, 346–350.

[58] Zhao, J. Q.; He, J. P.; Ding, X. C.; Zhou, J. H.; Ma, Y.; Wu, S. C.; Huang, R. M. A novel sol–gel synthesis route to NaVPO$_4$F as cathode material for hybrid lithium ion batteries. *J. Power Sources* **2010**, *195*, 6854–6859.

[59] Lu, Y.; Zhang, S.; Li, Y.; Xue, L. G.; Xu, G. J.; Zhang, X. W. Preparation and characterization of carbon-coated NaVPO$_4$F as cathode material for rechargeable sodium-ion batteries. *J. Power Sources* **2014**, *247*, 770–777.

[60] Ruan, Y. L.; Wang, K.; Song, S. D.; Han, X.; Cheng, B. W. Graphene modified sodium vanadium fluorophosphate as a high voltage cathode material for sodium ion batteries. *Electrochim. Acta* **2015**, *160*, 330–336.

[61] Xu, M. W.; Cheng, C. J.; Sun, Q. Q.; Bao, S. J.; Niu, Y. B.; He, H.; Li, Y. T.; Song, J. Correction: A 3D porous interconnected NaVPO$_4$F/C network: Preparation and performance for Na-ion batteries. *RSC Adv.* **2015**, *5*, 56686–566686.

[62] Jin, T.; Liu, Y. C.; Li, Y.; Cao, K. Z.; Wang, X. J.; Jiao, L. F. Electrospun NaVPO$_4$F/C nanofibers as self-standing cathode material for ultralong cycle life Na-ion batteries. *Adv. Energy Mater.* **2017**, *7*, 1700087.

[63] Chang, C. Y.; Li, Y.; He, W.; Li, G. B.; Guo, W. J.; Zhu, P. H.; Yao, M. M.; Feng, J. J. NaVPO$_4$F prepared under air as a cathode material for sodium-ion batteries. *Mater. Lett.* **2017**, *209*, 82–85.

[64] Feng, P. Y.; Wang, W.; Hou, J.; Wang, K. L.; Cheng, S. J.; Jiang, K. A 3D coral-like structured NaVPO$_4$F/C constructed by a novel synthesis route as high-performance cathode material for sodium-ion battery. *Chem. Eng. J.* **2018**, *353*, 25–33.

[65] Cheng, B.; Zhang, S. J.; Zou, F. X.; Luo, L. L.; Chen, Y. X.; Chen, S. J.; Zhuo, H. T.; Zeng, X. R. Nano-NaVPO$_4$F enwrapped in reduced graphene oxide as a cathode material for long-cycle and high-rate sodium-ion batteries. *J. Alloys Compd.* **2019**, *811*, 151828.

[66] Ge, X. C.; Li, X. H.; Wang, Z. X.; Guo, H. J.; Yan, G. C.; Wu, X. W.; Wang, J. X. Facile synthesis of NaVPO$_4$F/C cathode with enhanced interfacial conductivity towards long-cycle and high-rate sodium-ion batteries. *Chem. Eng. J.* **2019**, *357*, 458–462.

[67] Ling, M. X.; Li, F.; Yi, H. M.; Li, X. F.; Hou, G. J.; Zheng, Q.; Zhang, H. M. Superior Na-storage performance of molten-state-blending-synthesized monoclinic NaVPO$_4$F nanoplates for Na-ion batteries. *J. Mater. Chem. A* **2018**, *6*, 24201–24209.

[68] Chen, C. C.; Li, T. J.; Tian, H.; Zou, Y. B.; Sun, J. C. Building highly stable and industrial NaVPO$_4$F/C as bipolar electrodes for high-rate symmetric rechargeable sodium-ion full batteries. *J. Mater. Chem. A* **2019**, *7*, 18451–18457.

[69] Le Meins, J. M.; Crosnier-Lopez, M. P.; Hemon-Ribaud, A.;

Courbion, G. Phase transitions in the $Na_3M_2(PO_4)_2F_3$ family (M = Al^{3+}, V^{3+}, Cr^{3+}, Fe^{3+}, Ga^{3+}): Synthesis, thermal, structural, and magnetic studies. *J. Solid State Chem.* **1999**, *148*, 260–277.

[70] Sauvage, F.; Quarez, E.; Tarascon, J. M.; Baudrin, E. Crystal structure and electrochemical properties vs. Na^+ of the sodium fluorophosphate $Na_{1.5}VOPO_4F_{0.5}$. *Solid State Sci.* **2006**, *8*, 1215–1221.

[71] Massa, W.; Yakubovich, O. V.; Dimitrova, O. V. Crystal structure of a new sodium vanadyl(IV) fluoride phosphate $NA_3\{V_2O_2F[PO_4]_2\}$. *Solid State Sci.* **2002**, *4*, 495–501.

[72] Gover, R. K. B.; Bryan, A.; Burns, P.; Barker, J. The electrochemical insertion properties of sodium vanadium fluorophosphate, $Na_3V_2(PO_4)_2F_3$. *Solid State Ionics* **2006**, *177*, 1495–1500.

[73] Jiang, T.; Chen, G.; Li, A.; Wang, C. Z.; Wei, Y. J. Sol–gel preparation and electrochemical properties of $Na_3V_2(PO_4)_2F_3$/C composite cathode material for lithium ion batteries. *J. Alloys Compd.* **2009**, *478*, 604–607.

[74] Shakoor, R. A.; Seo, D. H.; Kim, H.; Park, Y. U.; Kim, J.; Kim, S. W.; Gwon, H.; Lee, S.; Kang, K. A combined first principles and experimental study on $Na_3V_2(PO_4)_2F_3$ for rechargeable Na batteries. *J. Mater. Chem.* **2012**, *22*, 20535–20541.

[75] Tsirlin, A. A.; Nath, R.; Abakumov, A. M.; Furukawa, Y.; Johnston, D. C.; Hemmida, M.; Krug Von Nidda, H. A.; Loidl, A.; Geibel, C.; Rosner, H. Phase separation and frustrated square lattice magnetism of $Na_{1.5}VOPO_4F_{0.5}$. *Phys. Rev. B* **2011**, *84*, 014429.

[76] Serras, P.; Palomares, V.; Goñi, A.; Gil De Muro, I.; Kubiak, P.; Lezama, L.; Rojo, T. High voltage cathode materials for Na-ion batteries of general formula $Na_3V_2O_{2x}(PO_4)_2F_{3-2x}$. *J. Mater. Chem.* **2012**, *22*, 22301–22308.

[77] Serras, P.; Palomares, V.; Alonso, J.; Sharma, N.; López del Amo, J. M.; Kubiak, P.; Fdez-Gubieda, M. L.; Rojo, T. Electrochemical Na extraction/insertion of $Na_3V_2O_{2x}(PO_4)_2F_{3-2x}$. *Chem. Mater.* **2013**, *25*, 4917–4925.

[78] Park, Y. U.; Seo, D. H.; Kim, H.; Kim, J.; Lee, S.; Kim, B.; Kang, K. A family of high-performance cathode materials for Na-ion batteries, $Na_3(VO_{1-x}PO_4)_2F_{1+2x}$ ($0 \leq x \leq 1$): Combined first-principles and experimental study. *Adv. Funct. Mater.* **2014**, *24*, 4603–4614.

[79] Liu, Z. G.; Hu, Y. Y.; Dunstan, M. T.; Huo, H.; Hao, X. G.; Zou, H.; Zhong, G. M.; Yang, Y.; Grey, C. P. Local structure and dynamics in the Na ion battery positive electrode material $Na_3V_2(PO_4)_2F_3$. *Chem. Mater.* **2014**, *26*, 2513–2521.

[80] Bianchini, M.; Brisset, N.; Fauth, F.; Weill, F.; Elkaim, E.; Suard, E.; Masquelier, C.; Croguennec, L. $Na_3V_2(PO_4)_2F_3$ revisited: A high-resolution diffraction study. *Chem. Mater.* **2014**, *26*, 4238–4247.

[81] Bianchini, M.; Fauth, F.; Brisset, N.; Weill, F.; Suard, E.; Masquelier, C.; Croguennec, L. Comprehensive investigation of the $Na_3V_2(PO_4)_2F_3$-$NaV_2(PO_4)_2F_3$ system by operando high resolution synchrotron X-ray diffraction. *Chem. Mater.* **2015**, *27*, 3009–3020.

[82] Broux, T.; Bamine, T.; Fauth, F.; Simonelli, L.; Olszewski, W.; Marini, C.; Ménétrier, M.; Carlier, D.; Masquelier, C.; Croguennec, L. Strong impact of the oxygen content in $Na_3V_2(PO_4)_2F_{3-y}O_y$ ($0 \leq y \leq 2$) on its structural and electrochemical properties. *Chem. Mater.* **2016**, *28*, 7683–7692.

[83] Liu, Q.; Meng, X.; Wei, Z. X.; Wang, D. X.; Gao, Y.; Wei, Y. J.; Du, F.; Chen, G. Core/double-shell structured $Na_3V_2(PO_4)_2F_3$@C nanocomposite as the high power and long lifespan cathode for sodium-ion batteries. *ACS Appl. Mater. Interfaces* **2016**, *8*, 31709–31715.

[84] Zhu, C. B.; Wu, C.; Chen, C. C.; Kopold, P.; Van Aken, P. A.; Maier, J.; Yu, Y. A high power-high energy $Na_3V_2(PO_4)_2F_3$ sodium cathode: Investigation of transport parameters, rational design and realization. *Chem. Mater.* **2017**, *29*, 5207–5215.

[85] Broux, T.; Fauth, F.; Hall, N.; Chatillon, Y.; Bianchini, M.; Bamine, T.; Leriche, J. B.; Suard, E.; Carlier, D.; Reynier, Y. et al. High rate performance for carbon-coated $Na_3V_2(PO_4)_2F_3$ in Na-ion batteries. *Small Methods* **2019**, *3*, 1800215.

[86] Yi, H. M.; Lin, L.; Ling, M. X.; Lv, Z. Q.; Li, R.; Fu, Q.; Zhang, H. M.; Zheng, Q.; Li, X. F. Scalable and economic synthesis of high-performance $Na_3V_2(PO_4)_2F_3$ by a solvothermal-ball-milling method. *ACS Energy Lett.* **2019**, *4*, 1565–1571.

[87] Zhang, B.; Dugas, R.; Rousse, G.; Rozier, P.; Abakumov, A. M.; Tarascon, J. M. Insertion compounds and composites made by ball milling for advanced sodium-ion batteries. *Nat. Commun.* **2016**, *7*, 10308.

[88] Mukherjee, A.; Sharabani, T.; Perelshtein, I.; Noked, M. Three-sodium ion activity of a hollow spherical $Na_3V_2(PO_4)_2F_3$ cathode: Demonstrating high capacity and stability. *Batter. Supercaps* **2020**, *3*, 52–55.

[89] Fang, R. H.; Olchowka, J.; Pablos, C.; Camacho, P. S.; Carlier, D.; Croguennec, L.; Cassaignon, S. Effect of the particles morphology on the electrochemical performance of $Na_3V_2(PO_4)_2F_{3-y}O_y$. *Batter. Supercaps* **2022**, *5*, e202100179.

[90] Essehli, R.; Yahia, H. B.; Amin, R.; Li, M. Y.; Morales, D.; Greenbaum, S. G.; Abouimrane, A.; Parejiya, A.; Mahmoud, A.; Boulahya, K. et al. Sodium rich vanadium oxy-fluorophosphate—$Na_{3.2}Ni_{0.2}V_{1.8}(PO_4)_2F_2O$—as advanced cathode for sodium ion batteries. *Adv. Sci.*, in press, https://doi.org/10.1002/advs.202301091.

[91] Liang, Z. T.; Zhang, X. F.; Liu, R.; Ortiz, G. F.; Zhong, G. M.; Xiang, Y. X.; Chen, S. J.; Mi, J. X.; Wu, S. Q.; Yang, Y. New dimorphs of $Na_5V(PO_4)_2F_2$ as an ultrastable cathode material for sodium-ion batteries. *ACS Appl. Energy Mater.* **2020**, *3*, 1181–1189.

[92] Mazumder, M.; Pati, S. K. Theoretical insights into $Na_5M(PO_4)_2F_2$ (M = Cr, V): A fluorophosphate-based high-performance cathode system for sodium-ion batteries. *J. Phys. Chem. C* **2021**, *125*, 19593–19599.

[93] Barpanda, P.; Chotard, J. N.; Recham, N.; Delacourt, C.; Ati, M.; Dupont, L.; Armand, M.; Tarascon, J. M. Structural, transport, and electrochemical investigation of novel $AMSO_4F$ (A = Na, Li; M = Fe, Co, Ni, Mn) metal fluorosulphates prepared using low temperature synthesis routes. *Inorg. Chem.* **2010**, *49*, 7401–7413.

[94] Ati, M.; Sougrati, M. T.; Recham, N.; Barpanda, P.; Reynaud, M.; Delacourt, C.; Armand, M.; Jumas, J. C.; Tarascon, J. M. Synthesis of new fluorosulphate materials using different approaches. *ECS Trans.* **2019**, *35*, 57–63.

[95] Tripathi, R.; Ramesh, T. N.; Ellis, B. L.; Nazar, L. F. Scalable synthesis of tavorite $LiFeSO_4F$ and $NaFeSO_4F$ cathode materials. *Angew. Chem., Int. Ed.* **2010**, *49*, 8738–8742.

[96] Ati, M.; Dupont, L.; Recham, N.; Chotard, J. N.; Walker, W. T.; Davoisne, C.; Barpanda, P.; Sarou-Kanian, V.; Armand, M.; Tarascon, J. M. Synthesis, structural, and transport properties of novel bihydrated fluorosulphates $NaMSO_4F \cdot 2H_2O$ (M = Fe, Co, and Ni). *Chem. Mater.* **2010**, *22*, 4062–4068.

[97] Reynaud, M.; Barpanda, P.; Rousse, G.; Chotard, J. N.; Melot, B. C.; Recham, N.; Tarascon, J. M. Synthesis and crystal chemistry of the $NaMSO_4F$ family (M = Mg, Fe, Co, Cu, Zn). *Solid State Sci.* **2012**, *14*, 15–20.

[98] Barpanda, P.; Ati, M.; Recham, N.; Chotard, J. N.; Walker, W.; Armand, M.; Tarascon, J. M. Crystal structure and electrochemical study of $A(Fe_{1-x}M_x)SO_4F$ (A = Li/Na; M = Co/Ni/Mn) fluorosulfates prepared by low temperature ionothermal synthesis. *ECS Trans.* **2019**, *28*, 1–9.

[99] Momida, H.; Kitajou, A.; Okada, S.; Oguchi, T. First-principles study of X-ray absorption spectra in $NaFeSo_4F$ for exploring Na-ion battery reactions. *J. Phys. Soc. Japan* **2019**, *88*, 124709.

[100] Recham, N.; Rousse, G.; Sougrati, M. T.; Chotard, J. N.; Frayret, C.; Mariyappan, S.; Melot, B. C.; Jumas, J. C.; Tarascon, J. M. Preparation and characterization of a stable $FeSO_4F$-based framework for alkali ion insertion electrodes. *Chem. Mater.* **2012**, *24*, 4363–4370.

[101] Lander, L.; Rousse, G.; Abakumov, A. M.; Sougrati, M.; van Tendeloo, G.; Tarascon, J. M. Structural, electrochemical and magnetic properties of a novel $KFeSO_4F$ polymorph. *J. Mater. Chem. A* **2015**, *3*, 19754–19764.